JGR Atmospheres

RESEARCH ARTICLE
10.1029/2021JD035000

Lagrangian Coherent Structures and Vortex Formation in High Spatiotemporal-Resolution Satellite Winds of an Atmospheric Kármán Vortex Street

Tobias Günther[1], Ákos Horváth[2], Wayne Bresky[3], Jaime Daniels[4], and Stefan Alexander Buehler[2]

[1]Friedrich-Alexander-Universität Erlangen-Nürnberg, Erlangen, Germany, [2]Meteorological Institute, Universität Hamburg, Hamburg, Germany, [3]I. M. Systems Group, Rockville, MD, USA, [4]NOAA/NESDIS Center for Satellite Applications and Research, College Park, MD, USA

Key Points:

- Recently developed high-cadence geostationary satellite winds enable the Lagrangian analysis of unsteady island wake flows
- Good correspondence between Lagrangian Coherent Structures and observed cloud patterns indirectly confirms the fidelity of fluid dynamics
- Discussion of benefits and pitfalls of common flow visualization techniques for the analysis of fluid dynamics

Supporting Information:

Supporting Information may be found in the online version of this article.

Correspondence to:

T. Günther,
tobias.guenther@fau.de

Citation:

Günther, T., Horváth, Á., Bresky, W., Daniels, J., & Buehler, S. A. (2021). Lagrangian Coherent Structures and vortex formation in high spatiotemporal-resolution satellite winds of an atmospheric Kármán vortex street. *Journal of Geophysical Research: Atmospheres*, *126*, e2021JD035000. https://doi.org/10.1029/2021JD035000

Received 1 APR 2021
Accepted 19 SEP 2021

Author Contributions:

Conceptualization: Tobias Günther, Ákos Horváth
Methodology: Tobias Günther, Ákos Horváth
Resources: Ákos Horváth
Software: Tobias Günther
Visualization: Tobias Günther
Writing – original draft: Tobias Günther, Ákos Horváth
Writing – review & editing: Wayne Bresky, Jaime Daniels, Stefan Alexander Buehler

Abstract Recent advances in geostationary imaging have enabled the derivation of high spatiotemporal-resolution cloud-motion winds for the study of mesoscale unsteady flows. Due to the general absence of ground truth, the quality assessment of satellite winds is challenging. In the current limited practice, straightforward plausibility checks on the smoothness of the retrieved wind field or tests on aggregated trends such as the mean velocity components are applied for quality control. In this study, we demonstrate additional diagnostic tools based on feature extraction from the retrieved velocity field. Lagrangian Coherent Structures (LCS), such as vortices and transport barriers, guide and constrain the emergence of cloud patterns. Evaluating the alignment of the extracted LCS with the observed cloud patterns can potentially serve as a test of the retrieved wind field to adequately explain the time-dependent dynamics. We discuss the suitability and expressiveness of direct, geometry-based, texture-based, and feature-based flow visualization methods for the quality assessment of high spatiotemporal-resolution winds through the real-world example of an atmospheric Kármán vortex street and its laboratory archetype, the 2D cylinder flow.

1. Introduction

Vortex streets formed in the cloudy wake of mountainous islands are the analogs of the classic Kármán vortex street observed in laboratory bluff-body flows. Atmospheric vortex streets develop in conditions characterized by a well-mixed subcloud layer capped by a strong temperature inversion with a weaker stably stratified layer above and consist of mesoscale eddies, which span the entire marine boundary layer and have a nearly upright axis with no height variation in their properties (i.e., they are approximately 2D). Although the spatial arrangement (aspect ratio) of these spectacular vortex patterns has been studied ever since their first photographs were obtained at the dawn of the satellite era (e.g., Chopra & Hubert, 1965; Hubert & Krueger, 1962; Lyons & Fujita, 1968; Young & Zawislak, 2006), advances in modeling and observational capabilities have recently led to a renewed interest specifically in their dynamics. Numerical forecast models and large-eddy simulations are now capable of handling spatial grid resolutions at the lower end of the meso-gamma scale (2–20 km) in a sufficiently large domain (hundreds of kilometers on a side) required for the realistic modeling of island wakes (Heinze et al., 2012; Nunalee & Basu, 2014; Nunalee et al., 2015).

The spatial resolution of satellite wind retrievals has also reached the kilometer scale (2–8 km), at least in a research setting if not operationally, which allows to characterize the finer details of wake flows. The wind and vorticity field of atmospheric vortex streets was successfully measured by stereo cloud-motion winds from the Multiangle Imaging SpectroRadiometer (MISR; Horváth, 2013) and also by ocean surface winds from the Advanced Scatterometer (ASCAT; Vogelzang et al., 2017). These polar-orbiter instruments, however, only offer snapshots of the wind field. The latest generation geostationary imagers, in contrast, can provide high-cadence wind retrievals that capture the time evolution of the wake. Horváth et al. (2020) used the Advanced Baseline Imager (ABI) aboard Geostationary Operational Environmental Satellite-16 (GOES-16) to derive 6 km resolution cloud-motion winds at 5 min frequency, to characterize the wake oscillations and to measure vortex shedding, advection, and decay in the lee of Guadalupe Island.

High spatiotemporal-resolution winds represent both challenges and opportunities. The validation of satellite winds is difficult due to the general lack of ground truth and traditionally relies on comparisons against sparse radiosonde observations. In recent years, aircraft observations have also been used to evaluate derived winds, but even with this additional data source there are significant gaps in the in-situ measurement network. As a result, the quality control of operational satellite winds mostly relies on spatial and temporal self-consistency checks. The quality of retrievals is expressed by the level of vector, speed, and direction consistency between neighboring as well as between consecutive wind vectors (Holmlund et al., 2001). These quality control schemes were designed with coarser-resolution global forecast models in mind, which require a description of the slowly varying large-scale flow. They are, however, inapplicable to unsteady wake flows that are characterized by large wind variations on small spatial and temporal scales, due to both small-scale dynamics and measurement uncertainties. Furthermore, the observation of local wind vectors alone does not allow flow comparison on the scale of features such as vortices, as soon as those are in motion, because of the superimposed transport (Günther & Theisel, 2018).

The effective visualization of high-resolution winds is also challenging. Traditional vector plots (wind barbs or arrows) are unsuitable for time-dependent flow, due to their inability to separate features from the underlying motion. In addition, spatially dense data sets suffer from occlusion of vectors. There are, however, alternative techniques that are similarly easy to calculate, yet are more informative, as they reveal underlying transport dynamics much more clearly. For example, a user survey of 2D vector field visualization methods found that techniques representing integral curves and conceptualizing particle advection tend to perform better in time-varying flows (Laidlaw et al., 2005). Recently, Bujack and Middel (2020) pointed out that atmospheric flows are visualized almost exclusively by basic techniques only (arrows, streamlines, or color coding the velocity magnitude) and recommended the more regular use of feature-based methods.

We believe there are opportunities for progress on both of these fronts. Complex spatiotemporal systems such as atmospheric vortex streets are highly structured, but nevertheless organize around a lower-dimensional skeleton of coherent features. We investigate selected techniques from direct, geometric, image-based, and feature-based flow visualization regarding their potential to serve as diagnostic measure, leading up to Lagrangian Coherent Structures (LCS; Haller, 2015), which identify the most attracting, most repelling, or least shearing material lines of particle dynamics. Such material boundaries, which can now be calculated thanks to the high-frequency of ABI winds, are of interest, because they segment the flow into compartments of coherent behavior.

Although these techniques are well-known in the fluid dynamics and scientific visualization literature, they have not yet caught on with the wider satellite wind community. Therefore, one of the goals of the current work is to serve as a practical tutorial, demonstrating these methods on the real-world vortex street wind data set of Horváth et al. (2020). Furthering this goal, we provide a MATLAB implementation of the discussed feature extraction methods as well as time series animations and scripts to reproduce the figures in the study.

In addition, we aim to show that LCS and particle/texture advection methods applied to the Guadalupe wind data visually describe the emergence of the observed cloud vortex patterns well and thus indirectly confirm the quality of the satellite wind retrievals. We argue that after further development, these techniques can serve as complementary tools for the quantitative validation, or at least consistency testing, of high spatiotemporal-resolution wind data. The atmospheric vortex street is a good case study, because we can also draw on and compare against well-known results obtained by the above techniques for the classic 2D cylinder flow.

The study is organized as follows. In Section 2, we introduce the notation used and briefly describe our measurement and simulation data. Section 3 describes the pitfalls of direct visualization methods, such as arrow plots. Section 4 elaborates on the calculation and use of geometric visualization methods that are centered around particle integration. Section 5 increases the information density by image-based techniques such as line integral convolutions. Section 6 takes a feature-centered approach to visualize the coherent structures in fluid flow. Finally, Section 7 concludes with an outline of opportunities for future work.

2. Background and Data

2.1. Notation

Throughout this work, we will refer to scalar numbers with italic letters, such as s. Vector-valued quantities are expressed with bold letters, such as $\mathbf{v}$. Matrices are denoted with capitalized bold letters, such as $\mathbf{J}$.

A vector field is a map $\mathbf{v}(\mathbf{x},t) = \mathbf{v}(x,y,t) : D \times T \to D$ that assigns each point $\mathbf{x} \in D$ in the *two*-dimensional domain $D \subset \mathcal{R}^2$ a vector:

$$\mathbf{v}(x,y,t) = \begin{pmatrix} u(x,y,t) \\ v(x,y,t) \end{pmatrix} \tag{1}$$

If $\mathbf{v}$ depends on time it is called unsteady or time-dependent. Otherwise, the flow is called steady, that is, when the time partial derivative vanishes to zero: $\frac{\partial}{\partial t}\mathbf{v} = \mathbf{0}$.

We explain all visualization methods through the examples of (a) a numerically simulated 2D vector field of the classic cylinder flow and (b) a satellite-retrieved real-world quasi-2D meteorological vector field containing an atmospheric Kármán vortex street. In the following, we give a brief description of the data sets and explain the first visualization method.

2.2. Data Sets

2.2.1. Cylinder2D Flow

For reference, we apply the visualization methods to the well-known laboratory Kármán vortex street. This fluid flow was numerically simulated with the open source solver Gerris (Popinet, 2003). The spatial domain $[-0.5,7.5] \times [-0.5,0.5]$ is filled with a viscous 2D fluid that is injected from the left into a channel with solid walls and slip boundary conditions. A circular obstacle is placed at (0,0) with radius 0.0625. The kinematic viscosity is $\nu = 0.00078125$, leading to a Reynolds number of $\mathrm{Re} = 160$. The data set is discretized onto a 640×80 grid and the time range $[0,15]$ is discretized with 1,501 time steps. The velocity vector field is publicly available; for more details on its definition we refer to Günther, Gross, et al. (2017a). Figure 1a shows the periodic patterns forming in the wake of the cylinder. Arrows do not align with the flow structures (shown in white), which are instead revealed by visualizing structures that tracer particles are attracted to, that is, locations at which smoke would collect if it was released from the cylinder. The white structures are calculated by the (backward) finite-time Lyapunov exponent (FTLE), which is explained later.

2.2.2. Guadalupe Flow

Satellite cloud-motion vectors (or "winds") were derived for the atmospheric Kármán vortex street observed by GOES-16 in marine stratocumulus in the lee of Guadalupe Island off Baja California on May 9, 2018. For later reference, the reflectance map is displayed in Figure 2. The stratocumulus deck was located below the top of a low-level temperature inversion starting at a base height of 570 m, with cloud top heights varying between 600 and 900 m and having a median value of 750 m. The cloud-motion vectors thus represent horizontal winds within a narrow layer (at a nearly constant level) and were extracted from 0.5 km resolution red band (0.64 μm) imagery provided by ABI every 5 min. Retrievals were generated from consecutive image pairs for the 8-hr period between 14:32 and 22:37 UTC, totaling 96 time steps and covering a 602×602-pixel domain encompassing Guadalupe and its wake down to 26 N latitude. A 5×5-pixel ($\sim 2.5 \times 2.5\,\mathrm{km}^2$) subscene was centered on each pixel in this domain and tracked forward in time by minimizing the sum of squared difference similarity measure between the target image subscene and the search image subscene (Bresky et al., 2012; Daniels et al., 2010). The resulting 2.5 km resolution local winds were then resampled onto a Universal Transverse Mercator (UTM) grid with a spacing of 6.3 km. To reduce noise, each UTM gridbox was assigned the median of the local wind vectors it contained. For more details, including a public link to the data repository, see Horváth et al. (2020).

An arrow plot of the island wake is shown in Figure 1b. Note that the arrows do not reveal the mushroom patterns visible in the clouds, since the arrow direction depends not only on the local motion indicated by the vortex pattern but also on its transport. Namely, the arrow direction is a superposition of flow features (e.g., vortical motion inside vortices) and the ambient transport (overall transport tendency). Thus, arrows

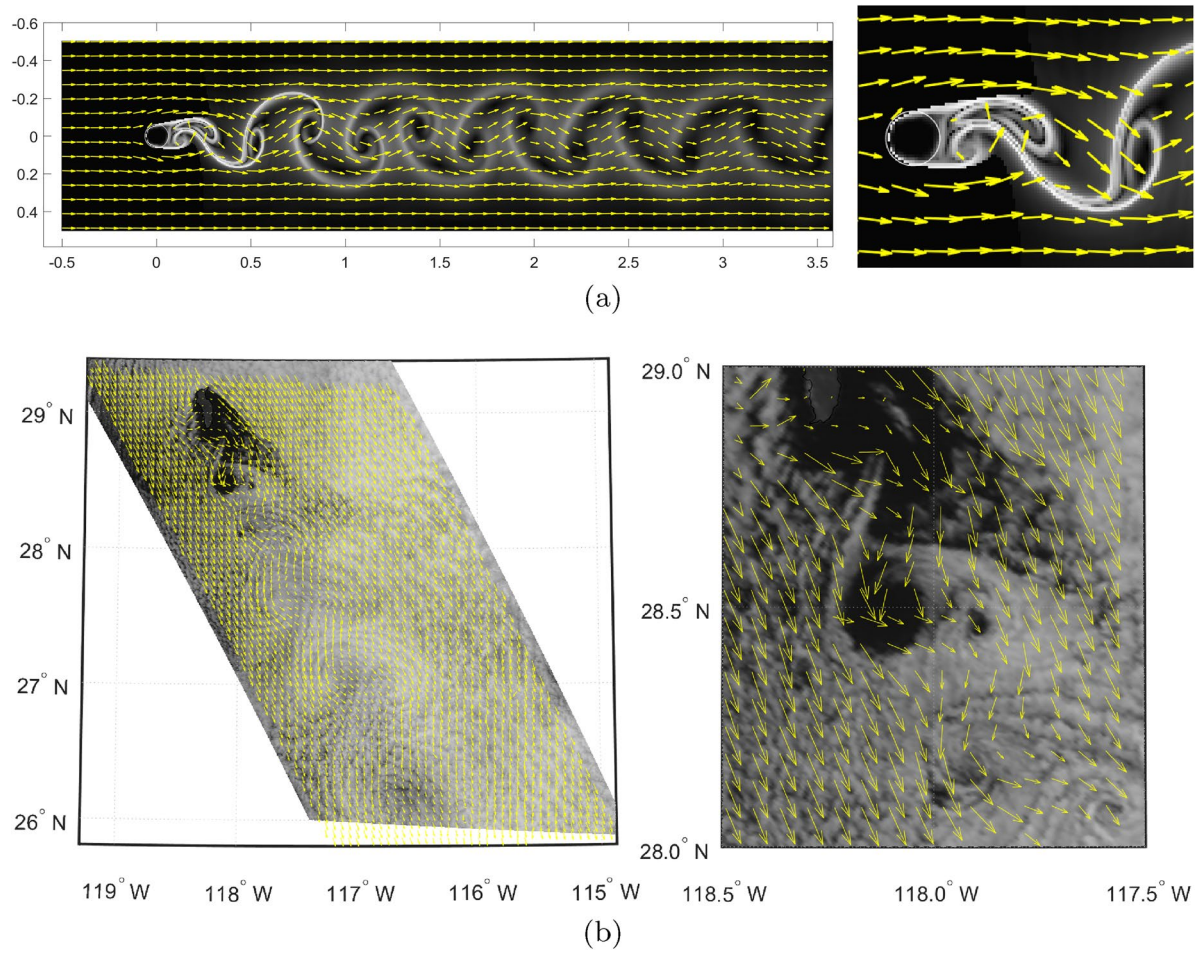

Figure 1. Arrow plots of the Cylinder2D flow at $t = 7.5$ (a) and the Guadalupe flow at 17:03 UTC (b). The left image shows the full domain and the right image presents a close-up view of the leeward side of the obstacle.

are unsuitable to study the correlation with the observed imagery. The satellite-retrieved data exhibit occasional outliers with exceptionally high wind speed and strong deviation from surrounding vectors. In Horváth et al. (2020), the vertical component of relative vorticity calculated from the horizontal winds was smoothed with a simple 3×3 gridbox averaging window to reduce the effect of outliers. In the current study, we preprocess the flow using an energy-based smoothing, which is equivalent to a masked isotropic diffusion that is parameterized through a compromise between data similarity and smoothness rather than the specification of a filter size.

Let $\mathcal{D}$ be the spatial domain of the data and let $\mathcal{M} \subset \mathcal{D}$ be the part of the domain inwhich the velocity values are available and not marked as outlier, that is, the absolute value of both velocity components is below $8m/sec$, a threshold we chose empirically. Given the original vector field $\mathbf{v}(\mathbf{x},t)$ at each given time t, we minimize the following energy E to solve for a new vector field $\mathbf{v}^*(\mathbf{x},t)$ such that

$$E = \underbrace{\int_{\mathcal{M}} \|\mathbf{v}(\mathbf{x},t) - \mathbf{v}^*(\mathbf{x},t)\|^2 \partial\mathbf{x}}_{\text{data similarity}} + \underbrace{\lambda \int_D \left\| \frac{\partial \mathbf{v}^*(\mathbf{x},t)}{\partial \mathbf{x}} \right\|^2 \partial\mathbf{x}}_{\text{smoothness}} \rightarrow \min \tag{2}$$

Since the above energy is quadratic in its unknowns, it has one optimal solution that can be found by discretizing the domain and performing a linear least squares fit. Here, we fit a vector field to the satellite winds, wherever they are available, and we generally assume that the desired vector field is smooth, which is known as Tikhonov regularization. The parameter λ is thereby a smoothness weight, which we empirically set to $\lambda = 0.2$. Selecting the weight is a compromise between numerical stability and correctness in

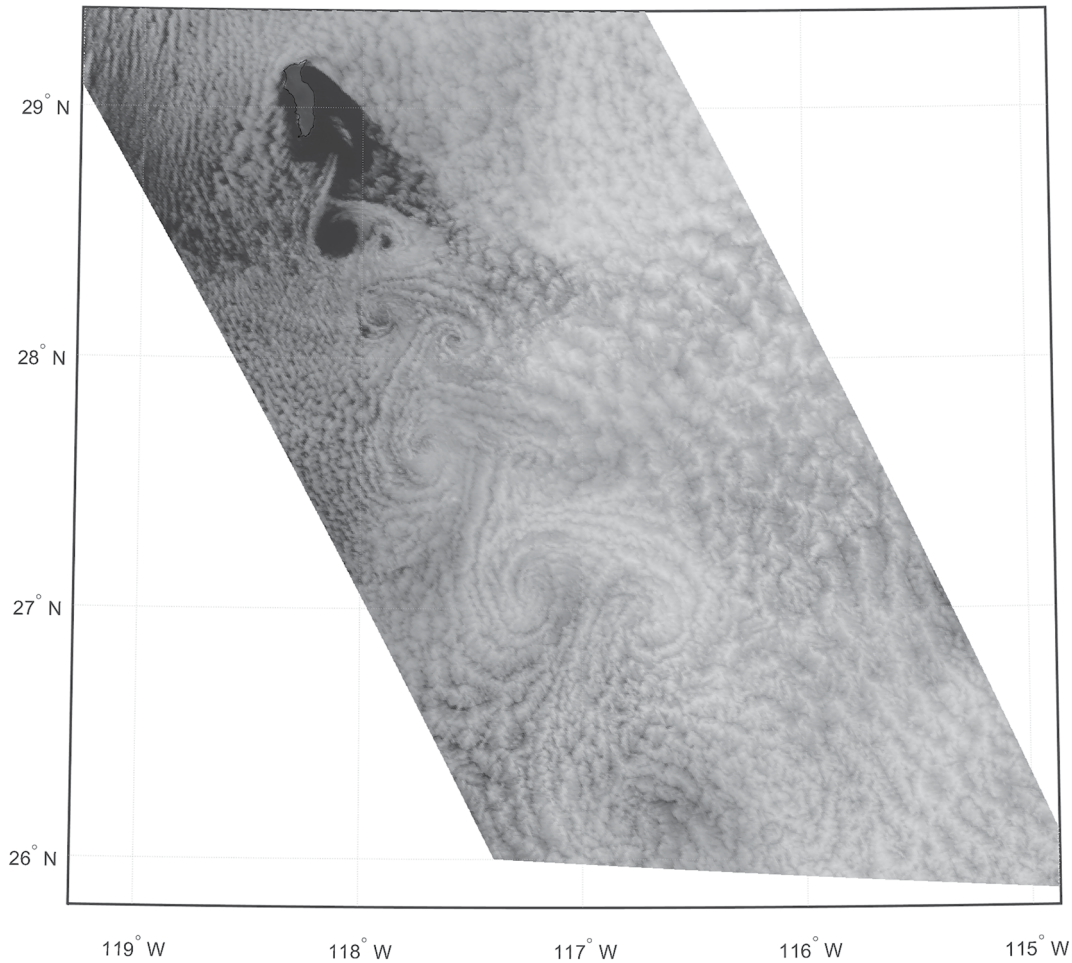

Figure 2. For better comparison with various flow visualization techniques later on, we provide the reflectance map of the Guadalupe flow for May 9, 2018, 17:03 UTC.

the location of extracted features. Compared to the smoothing of Horváth et al. (2020), our Tikhonov-based smoothing first removes outliers to not propagate false values into the neighborhood.

3. Direct Methods

Direct visualization methods encode components of the vector field by color or place glyphs at discrete locations to convey derived information. For general vector field data, the most commonly used glyph is an arrow that depicts the wind direction; for the special case of meteorological wind fields an alternative is the wind barb. For a comprehensive introduction to glyph-based techniques, we refer to the survey of Borgo et al. (2013).

3.1. Arrow Plots

Arrow plots visualize a vector field by placing a small arrow at each data grid point, indicating the direction of the flow using the arrow direction and the magnitude of the vector by the length of the arrow. Examples can be seen in Figure 1. Care must be taken not to make the arrows too long, as they start to overlap otherwise. Because the exact magnitude might be difficult to discern when viewing vectors, meteorologists often prefer the use of wind barbs, which consist of a fixed-length shaft indicating direction and a combination of short and long barbs and pennants (collectively "feathers") to indicate speed. Wind barb overlap, however, is even more of an issue for dense vector fields, due to the presence of the "feathers". In interactive

visualization applications, the number of arrows can be increased when the user zooms in to maintain a constant arrow density.

3.2. Discussion

An arrow plot is generally ineffective in showing a time-dependent fluid flow phenomenon. In Figure 1a, for instance, the location of vortices and other fluid flow features is not apparent from the visualization. Arrow plots can therefore not form the basis of conclusions about flow behavior. The continuum mechanical reason for this is that the physical interpretation of the vector orientation and length is not objective (Truesdell & Noll, 1965). Intuitively, lacking objectivity means that two different observers, for example one standing still and another one performing a rotation, might draw different conclusions when observing the same physical phenomenon, which is highly undesirable. Objectivity is a mathematical property that is obtained when a measure is invariant under uniform rotations and translations of the reference frame, that is, all observers will draw the same conclusion. Formally, let $\mathbf{v}(\mathbf{x}, t)$ be a vector-valued property observed in frame $\mathcal{F}_1$ and $\mathbf{w}(\mathbf{y}, t)$ be the same vector-valued property observed in frame $\mathcal{F}_2$ that is moving relative to $\mathcal{F}_1$ by a Euclidean transformation:

$$\mathbf{y} = \mathbf{Q}(t)\,\mathbf{x} + \mathbf{c}(t), \tag{3}$$

where $\mathbf{Q}(t)$ is an arbitrary time-dependent rotation matrix, and $\mathbf{c}(t)$ is an arbitrary time-dependent translation vector. Then, the vector-valued property is objective if it fulfills:

$$\mathbf{w}(\mathbf{y}, t) = \mathbf{Q}(t)\,\mathbf{v}(\mathbf{x}, t). \tag{4}$$

Since arrow length and orientation are different for differently moving observers, arrows are not useful to study the behavior of particles in the fluid and their immediate value as quality metric in a vector field comparison is limited. Arrow plots can only reveal instantaneous structures, as for example needed in streamline-oriented topology (Günther & Baeza Rojo, 2021). Nevertheless, an arrow plot is a frequent first choice to get an initial impression of the vector data, for example to investigate the amount of noise present at individual grid points. A more sensible quality metric would inspect reference frame invariant features that are derived from the velocity field and would utilize the temporal coherence of those structures. In the following section, we take the first step in this direction by inspecting integral geometry that reveals patterns and may serve as structure along which coherence can be measured.

4. Geometric Methods

4.1. Flow Maps

In experimental flow visualization, a common approach to visualize a usually invisible fluid flow is to release tracers such as smoke or dye or hydrogen bubbles, which are advected by the flow, creating striking patterns (streaklines) that convey the motion of the fluid (Van Dyke, 1982). In atmospheric flows, this is partially mimicked by the observation of clouds, though their evolution is not strictly a matter of passive advection. Once vector fields are captured or numerically simulated, computational flow visualization provides a multitude of approaches to visualize the fluid flow structures, which identify the driving processes that govern the transport. We thereby distinguish between Eulerian approaches that analyze the flow per time step and Lagrangian approaches that derive an analysis from particle motion. Therefore, a key ingredient is the ability to trace virtual particles, which we cover below.

In an unsteady flow $\mathbf{v}(\mathbf{x}, t)$, that is, when the flow is changing over time, the trajectory $\mathbf{x}(t)$ of a massless tracer particle is called a pathline. For a given seed point $\mathbf{x}_0$ and seed time t_0, a pathline is the solution to the ordinary differential equation (ODE):

$$\frac{\mathrm{d}}{\mathrm{d}t}\mathbf{x}(t) = \mathbf{v}(\mathbf{x}(t), t) \quad \text{with} \quad \mathbf{x}(t_0) = \mathbf{x}_0, \tag{5}$$

that is, the pathline is always tangential to the flow. The trajectory is numerically calculated as an initial value problem for a given initial condition using:

$$\mathbf{x}(t) = \mathbf{x}(t_0) + \int_{t_0}^{t} \mathbf{v}(\mathbf{x}(\tau), \tau)\, d\tau \quad \text{with} \quad \mathbf{x}(t_0) = \mathbf{x}_0. \tag{6}$$

In an unsteady flow, each particle needs to store its current position and also its current time, since the vector field that describes where the particles goes next is time-dependent.

For notational convenience, it is common to introduce the flow map $\mathbf{\Phi}_{t_0}^{\tau}(\mathbf{x}_0) : D \rightarrow D$, which maps a particle seeded at location $\mathbf{x}_0$ at time t_0 to its destination after pathline integration for duration τ, cf., Haller (2015):

$$\mathbf{\Phi}_{t_0}^{\tau}(\mathbf{x}_0) = \mathbf{x}_0 + \int_{t_0}^{t_0+\tau} \mathbf{v}(\mathbf{x}(t), t)\, dt. \tag{7}$$

For our data sets, the flow maps are visualized in Figure 3. In these figures, the position that a particle reaches after numerical integration is color-coded directly. The x-component is mapped to the red channel and the y-component is mapped to the green channel. For an integration duration of $\tau = 0$, as for the Cylinder2D flow in Figure 3a (top), no particle has moved yet and thus we directly color-code the seed point location. However, it is remarkable that the vortex pattern immediately becomes apparent when visualizing the flow map after a short integration, as in Figure 3a (bottom). Here, the white areas denote locations from which the particle has left the domain during numerical integration. Thus, here the flow map is undefined. Similarly, the vortex pattern also becomes apparent in the Guadalupe flow in Figure 3b. The flow map is rarely visualized directly apart from debugging purposes. Instead structures and features are derived from it, which enables more quantification and guidance of attention, for instance for the detection of transport barriers and vortices. We will describe those approaches later in Section 6 in more detail.

4.2. Integral Curves

Throughout the flow visualization literature, we can find a number of different line geometries that are used to study particle motion (McLoughlin et al., 2010). The trajectories of particles in a fluid flow are generally referred to as integral (or characteristic) curves, referring to the integral formulation of the ODE that defines them, see for example Equation 6. Depending on the type of fluid flow–steady or unsteady–different kinds of integral curves arise that have different meaning. In geometry-based flow visualization, we primarily distinguish four types of integral curves, which are illustrated in Figure 4a for the flow behind a Cylinder and in Figure 4b for the Guadalupe flow. In both cases, we would like a Kármán vortex street to appear. In the following, we will investigate how well the various types of integral curves are able to reveal this flow pattern.

1. Streamlines are the tangent curves of steady vector fields, that is, $\frac{\mathrm{d}}{\mathrm{d}t}\mathbf{r}(t) = \mathbf{v}(\mathbf{r}(t))$ where $\mathbf{v}(\mathbf{x})$ is a steady (time-independent) vector field or a time slice of an unsteady flow. Usually, they are used to study instantaneous vector fields such as magnetic fields or truly steady flows. In a time-dependent flow, they are calculated per time slice, which is not physically meaningful. Since actual particles move forward in time, that is, the flow is temporally changing as the particles are traveling, streamlines do not correspond to the physical trajectory of a real particle. When plotting streamlines in an unsteady flow, flow patterns such as vortices might become apparent. It should, however, always be clear that these structures do not actually exist and they should not be the foundation of an argumentation in flow analysis.
2. Pathlines are defined as the solution to an initial value problem in Equation 6. Using the flow map in Equation 7, they are given by $\mathbf{p}(\tau) = \mathbf{\Phi}_{t_0}^{\tau}(\mathbf{x}_0)$ and describe the paths of massless particles in fluid flows. These lines are in fact the trajectories of individual particles and are therefore the preferred choice when studying transport properties in time-dependent vector fields. Similar to streamlines, these lines are the result of an ODE, cf., Equation 5. Note how neither streamlines nor pathlines are able to reveal the vortex street in the fluid flows. While it is generally not meaningful to view streamlines in time-dependent flows, it is not enough either to view pathlines when looking for flow patterns. A pathline is a series of locations that have been visited by a given particle at different moments in time. Pathlines are therefore not useful to depict flow patterns at one specific moment in time.
3. Streaklines, on the other hand, are used to reveal flow patterns at one specific moment in time. They are assembled by continuously releasing particles from a seed point $\mathbf{x}_0$ at different times and advecting all particles to the same time slice, which is referred to as the observation time t. Using the flow map in Equation 7, streaklines are defined as $\mathbf{s}(\tau) = \mathbf{\Phi}_{\tau}^{t-\tau}(\mathbf{x}_0)$. Conceptually, streaklines are the equivalent to the trail of smoke or ink released from a point source, which takes us much closer to experimental flow visualization methods. Note that streaklines are successful in revealing fluid flow patterns such as vortices,

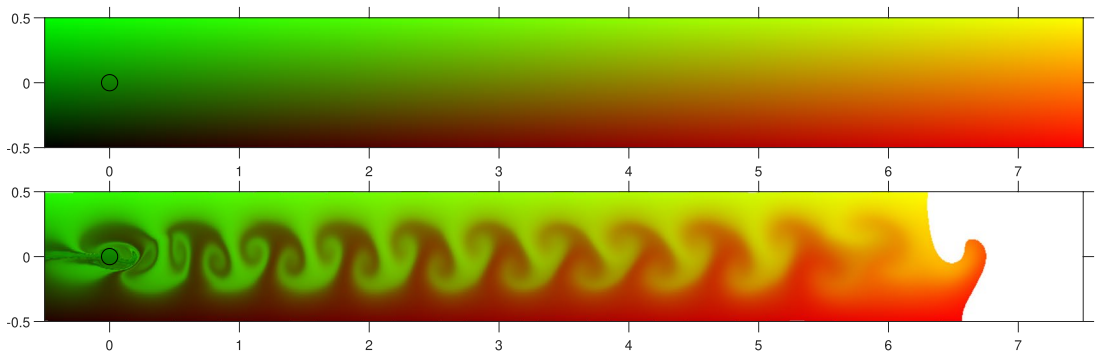

(a)

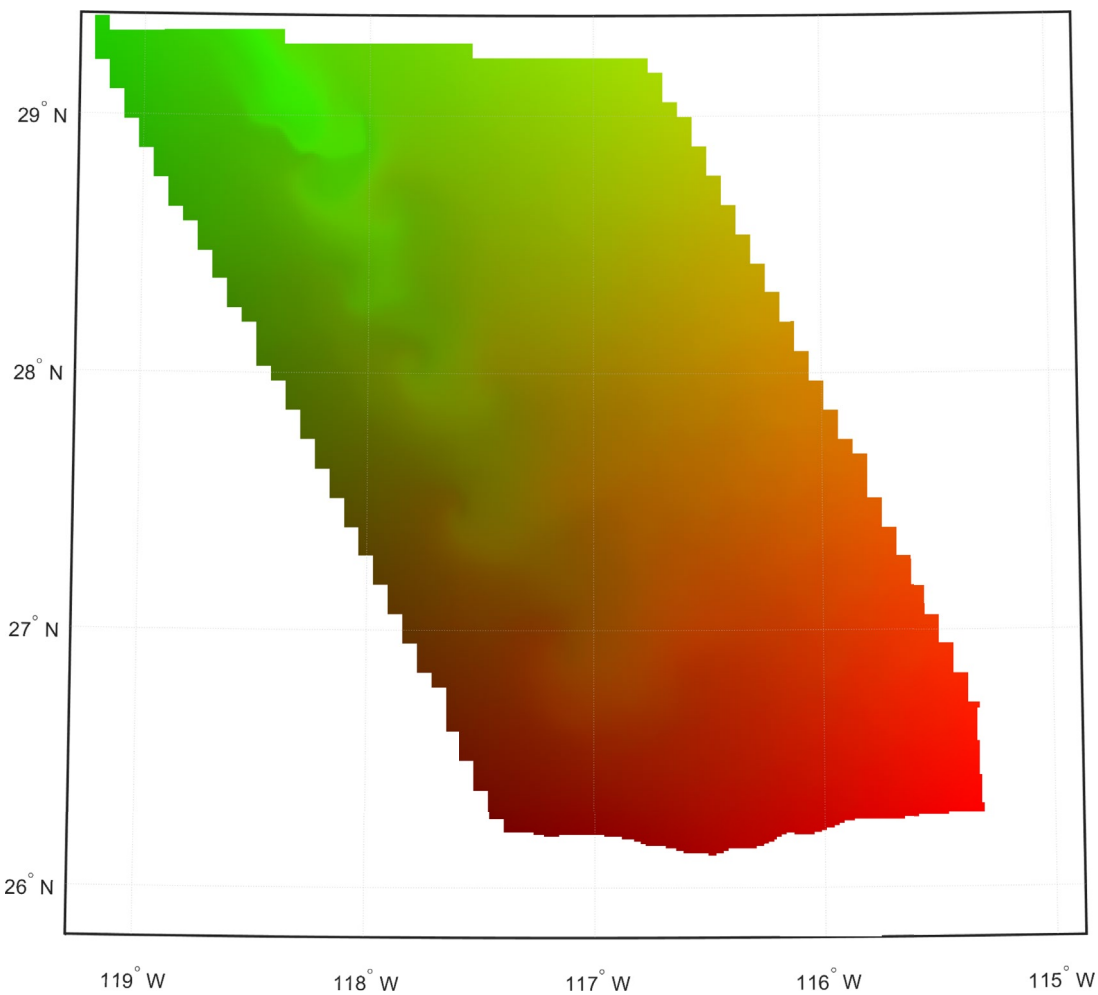

(b)

Figure 3. These flow map visualizations color-code at each pixel the coordinate that is reached after integration for a certain duration from that pixel. Here, the reached coordinates are visualized by color-coding the x- and y-coordinates with red and green. In (a), the Cylinder2D flow with duration $\tau = 0$ (top, only shown for reference to illustrate the color-coding) and $\tau = 1$ (bottom) are shown. In (b), the Guadalupe flow is depicted. After advection from $t_0 =$ 18:22 UTC for duration $\tau =$ 02:46:40 hr the flow structures become apparent.

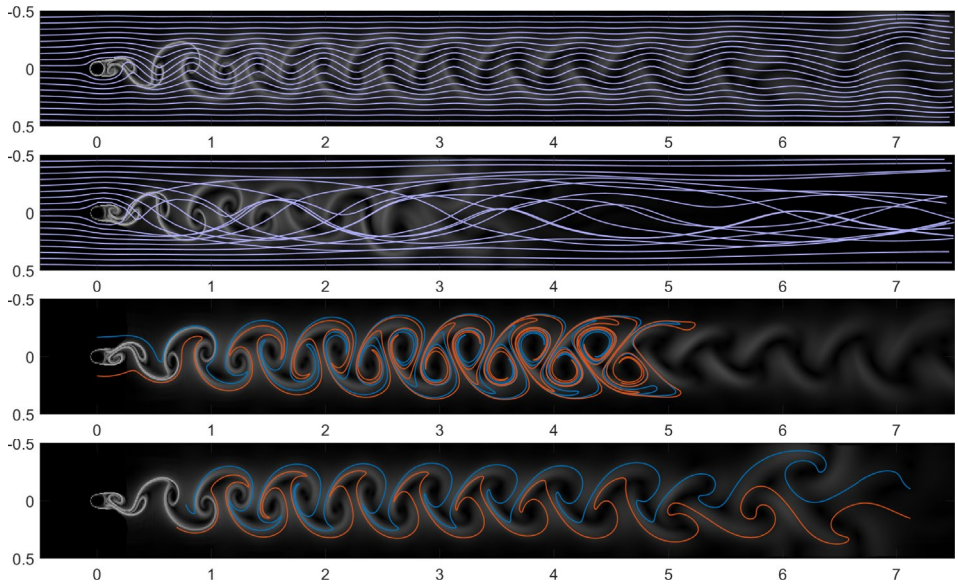

(a)

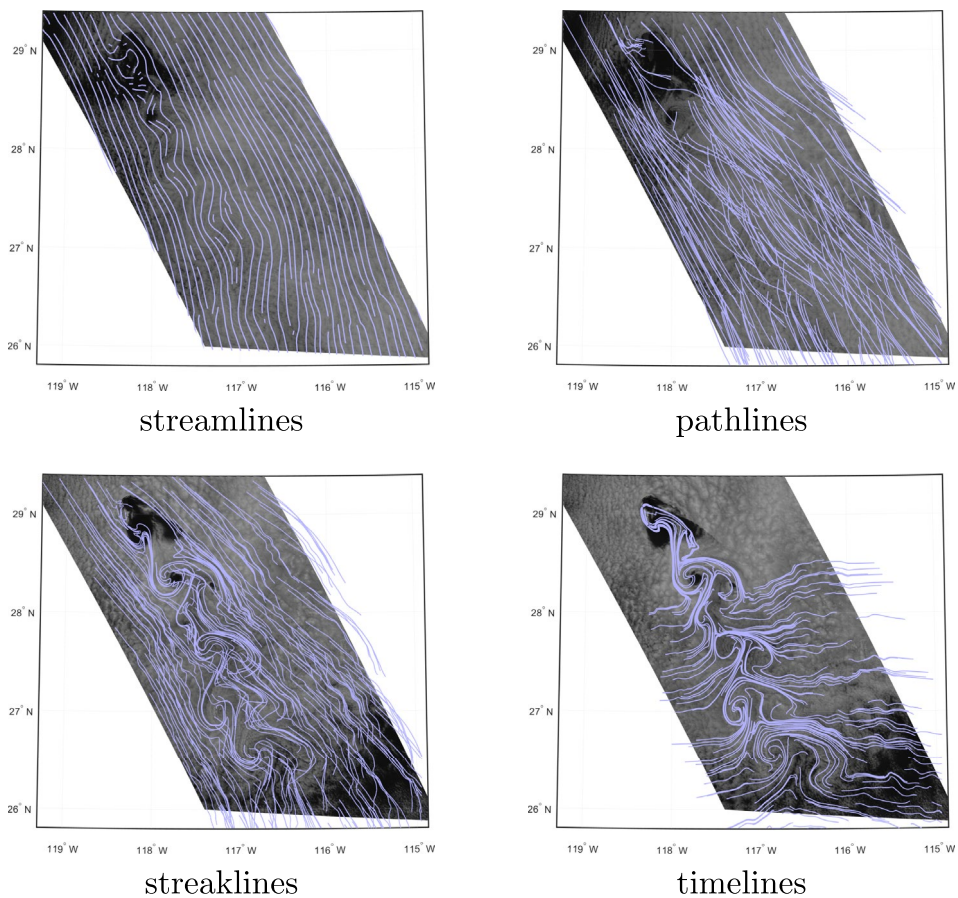

(b)

Figure 4. In (a), we see integral curves in the Cylinder2D flow, from top to bottom: streamlines ($t_0 = 10$, $\tau = 9$), pathlines ($t_0 = 6$, $\tau = 9$), streaklines ($t_0 = 7$, $\tau = 5$) and timelines ($t_0 = 8$, $\tau = 1.2$). Streaklines and timelines align with the flow patterns in the background. In (b), integral curves of the Guadalupe flow are shown ($t_0 =$ 15:55:20 UTC, $\tau =$ 06:06:40 UTC) with satellite images in the background (for streamlines and pathlines at start time t_0, and for streaklines and timelines at end time $t_0 + \tau$).

as long as the particles can reach those structures. Unlike streamlines and pathlines, which are computed by advecting a single particle, streaklines are computed by advecting a continuously growing list of particles forward in time. Whenever two subsequent particles are rapidly moving apart from each other, a new particle has to be inserted in-between them in order to maintain a sufficiently fine discretization of the streakline. Ideally, the new particle is inserted at the seed point and is traced up to the observation time. For simplicity, however, it is common to interpolate the new particle location at the observation time from the two particles that drifted too far apart, which is easier since it does not require access to previous time steps, but also introduces interpolation errors.

4. Timelines are curves that are advected over time. For a seeding curve $\mathbf{c}(u)$ at time t_0, the timeline at observation time $t_0 + \tau$ is $\mathbf{t}(u) = \mathbf{\Phi}_{t_0}^{\tau}(\mathbf{c}(u))$. Conceptually, timelines correspond to a line of ink that is injected at only one moment in time and then advected to the observation time. Similar to streaklines, particles on a timeline may separate away from each other, which requires an adaptive refinement. Both streaklines and timelines reveal physically meaningful flow patterns. The main difference between streaklines and timelines is in the analysis question they answer: how do particles evolve that were seeded at different times but from the same location (streaklines) versus how do particles evolve that were seeded at the same time but from different locations (timelines).

In practice, pathlines and streaklines are computed for unsteady vector fields only, whereas streamlines are computed for steady flows as well as for the individual time steps of unsteady flows. While it is conceptually possible to calculate pathlines and streaklines in steady flow, the resulting line geometry is identical to streamlines. It is worth mentioning that similar to streamlines and pathlines, streaklines and timelines can also be calculated as tangent curves in a lifted higher-dimensional vector field computed from the spatial and temporal gradients of the flow map (Weinkauf et al., 2012).

When visualizing line geometry, we generally aim for less line intersections (in 2D) and less line occlusions (in 3D) in order to avoid visual clutter (Günther, Theisel, et al., 2017). An advantage of streamlines is that they cannot intersect, since only one trajectory can pass through each point in the domain. When pathlines are plotted in space they can intersect, since particles may pass through the same location at different times from a different direction. We can observe such intersections in Figure 4. Streaklines will only intersect if a streakline sweeps over the seed point of another streakline. Self-intersections are also possible when the streakline particles move over their own seed point. Finally, timelines will intersect when their seed curves intersect. When using line geometry to reveal flow patterns, we not only need an integration algorithm, but we also need a good seed placement or line selection algorithm in order to avoid the aforementioned intersections and occlusions. Generally, these approaches are categorized into density-based (Jobard & Lefer, 1997; Mattausch et al., 2003) methods that evenly fill the domain with lines, feature-based (Ye et al., 2005; Yu et al., 2012) methods that place lines primarily around points of interest to ensure their visibility, and similarity-based (Chen et al., 2007) methods that avoid redundant lines that carry no additional information. For the streamlines in Figure 4, we used the placement algorithm of Jobard and Lefer (1997), which generates streamlines with uniform density. Such streamline seedings have also been the foundation for additional encodings along the lines such as the wind magnitude using glyphs (Pilar & Ware, 2013). We refer to Sane et al. (2020) for a recent survey.

4.3. Discussion

The various types of integral geometry have different strengths and weaknesses and should be applied accordingly. Shared among all types of geometry is the seeding problem and the potential visual clutter when showing too many lines. Streamlines and pathlines are not suitable when searching for coherent structures, as they cannot reveal cloud patterns. While streaklines are preferred in this case, they have the downside that the time and place of formation of the revealed structures is unclear. For example, the streaklines in Figure 4a show more structure further downstream than directly behind the cylinder. This is because the structures have accumulated over the life time of the particles. Once a structure has formed it will be advected further down the flow, making it unclear whether the implied rotating motion is still ongoing or whether the structure has been advected only. Timeline particles, on the other hand, have all been advected for the same amount of time, making the structures more comparable.

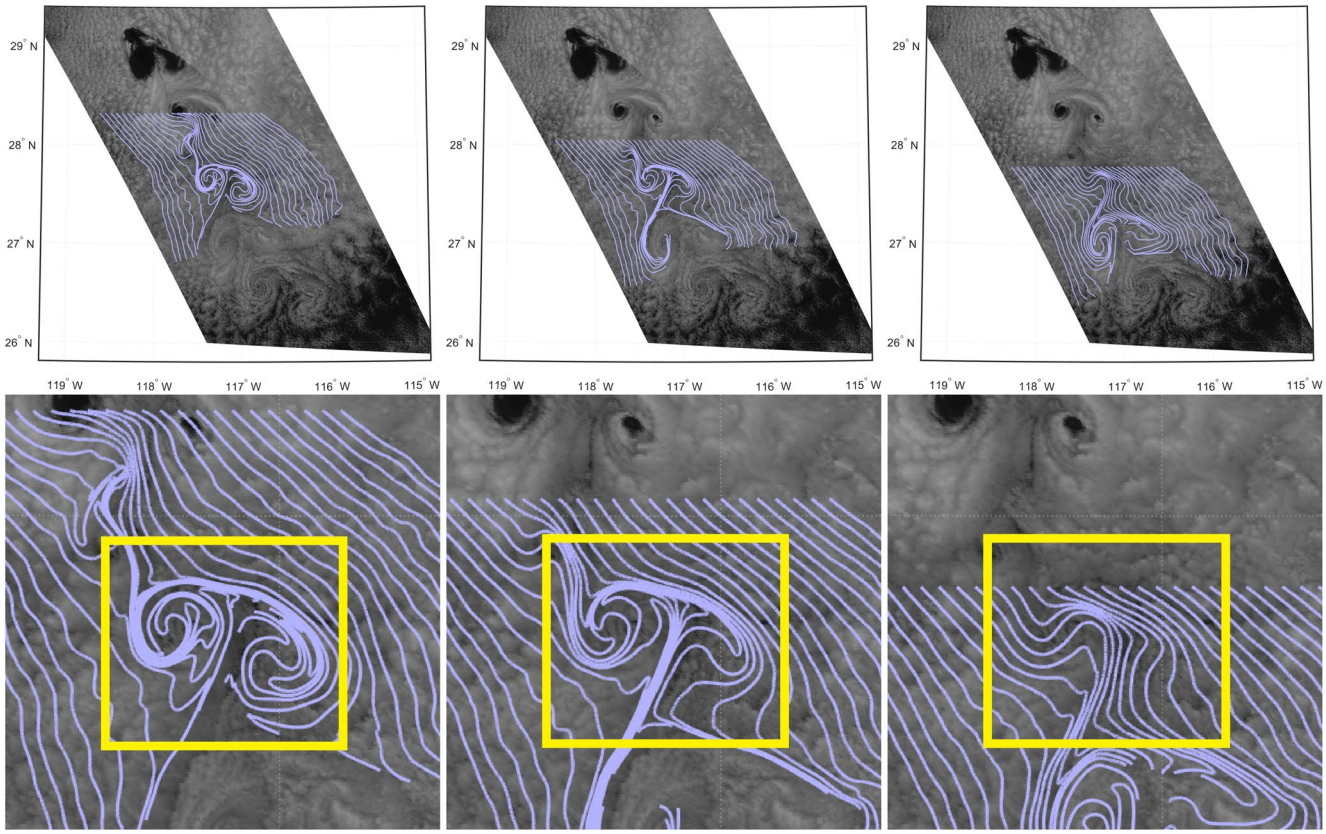

Figure 5. The geometric shape of streaklines is determined by the seeding location and the integration duration. The top row shows streaklines arising from three different seeding lines. Below, close-ups are displayed in which the same region is highlighted by the yellow box. In the left-most image, streakline particles in the box have been traced longer and thus accumulated more rotation than the streakline particles in the right-most image.

As Cimbala et al. (1988) pointed out, early experimental studies of bluff body wakes based on streakline photographs often arrived at erroneous conclusions about the local flow conditions due to this integrated memory effect. In order to accurately discern the flow at some location, the tracer source (smoke-wire, hydrogen bubble generator, or dye) must be placed at just the right distance upstream of that location (aka the seeding problem). If the source is too close to the observation point, the streaklines do not have enough time to deform. Figure 5 gives an example for such a setting in the Guadalupe flow, showing streaklines that were traced over the full time domain from different seeding lines, with the level of detail in the captured flow patterns clearly depending on how long the particles experienced rotating motion. Likewise if the source is too far upstream, the streakline pattern gets fixed and simply advects along with the mean flow. Laboratory streakline photographs may show well-defined vortex pairs far downstream of the obstacle, even though the local flow is nearly parallel. This is because vorticity decays at a much faster rate than smoke or dye diffuses. A similar disconnect between the visual appearance of far-wake cloud vortex patterns and vorticity also affects the Guadalupe flow, see later Section 6. An additional issue is line intersection. Streamlines can never intersect. Pathlines will intersect frequently, since they are assembled by particles living in different time steps. Streaklines will (self-)intersect whenever a streakline is advected over the seed point of another streakline–which is guaranteed to happen in any basic visualization tool without careful seed placement and streakline truncation–, and timelines will intersect when their initial seed curves intersect. The visual clutter caused by line intersection can be mitigated by truncating lines if their distance falls below a certain threshold.

5. Image-Based Methods

The previous geometry-based methods require the seeding of line geometry. Even when placing lines with an even spacing between them, there is still empty space between lines for which the flow behavior is not visualized, potentially missing details. In the following, texture-based methods are described, which encode information at every output pixel.

5.1. Texture Advection

A common approach to observe air and liquid flows in experimental flow visualization is by dye injection. Computationally, this can be reproduced by advecting a scalar field. The computational setting, however, allows us to inject patterns leading to more expressiveness. Since this advection is usually done on graphics processing units (GPUs), where scalar fields are best represented in texture memory, this technique is also known by the name texture advection. More formally, we can express the texture advection of a scalar field $s(\mathbf{x})$ with the flow map $\mathbf{\Phi}_{t_0}^{\tau}(\mathbf{x})$, cf., Section 4.1, by using

$$s(\mathbf{x}, t) = s(\mathbf{\Phi}_{t_0}^{t_0 - t}(\mathbf{x})) \tag{8}$$

which results in the time-dependent scalar field $s(\mathbf{x},t)$, which is equal to the initial texture at $t = t_0$. Conceptually, there are many different ways to implement the advection, such as numerically solving it as a partial differential equation (MacCormack, 2002), which would also allow for the modeling of effects like dissipation, or by taking a Lagrangian approach that advects a particle backwards to the seed time and fetches the texture value, as done in Equation 8. The latter method is illustrated in Figure 6, which is able to deform the texture, here a simple checkerboard pattern, without numerical dissipation. The black regions show locations from which the backward particle integration in Equation 8 left the flow domain. The deformation of individual squares becomes quickly apparent as they stretch under the repelling flow and roll up into vortices. In fact, structures emerge even when a noise texture is advected with the flow. Using patterns such as the checkerboard, we can also see where no deformation has occurred, which is less obvious in previous visualization methods. Note that edges in the checkerboard are timelines of the flow.

5.2. Line Integral Convolution

The line integral convolution (LIC) (Cabral & Leedom, 1993) is among the most common flow visualization methods, which is used to visualize the streamlines of a steady vector field $\mathbf{v}(\mathbf{x})$. Given a texture $T(\mathbf{x})$ with random noise values in [0,1] and a convolution kernel $k(s)$ with a support in $s \in [-l, l]$, the LIC computes a gray value image $I(\mathbf{x}_0)$ for every point $\mathbf{x}_0$ in the domain:

$$I(\mathbf{x}_0) = \int_{s_0 - l}^{s_0 + l} k(s - s_0) \cdot T(\mathbf{s}(s))\, \mathrm{d}s \tag{9}$$

where $\mathbf{s}(s)$ is the streamline released at $\mathbf{x}_0$ that is traced in forward and backward direction for length . Examples are shown in Figures 7a and 7b. Conceptually, the LIC integrates the noise values along a streamline, where the length of the streamline is a user parameter. For pixels located nearby on the same streamline, the integration accumulates almost identical noise values, resulting in very similar gray values along the streamline. Adjacent streamlines, however, sample an uncorrelated set of random values, resulting in a different gray value. It is important to note that the streamline should be arclength parameterized. If it were parameterized by the integration duration, too many identical noise values would be added once a streamline approaches a critical point or gets stuck at an obstacle, leading to noticeable artifacts and loss of visual contrast.

5.3. Discussion

The effectiveness of texture advections depends on the patterns that are advected, for example, the size of the squares of a checkerboard pattern. The larger the patterns, the less localized information becomes visible. While the shape of the advected squares informs the reader whether a deformation occurred or not, the display of non-deformed black and white squares still grabs attention through the display of edges that do not carry a particular meaning.

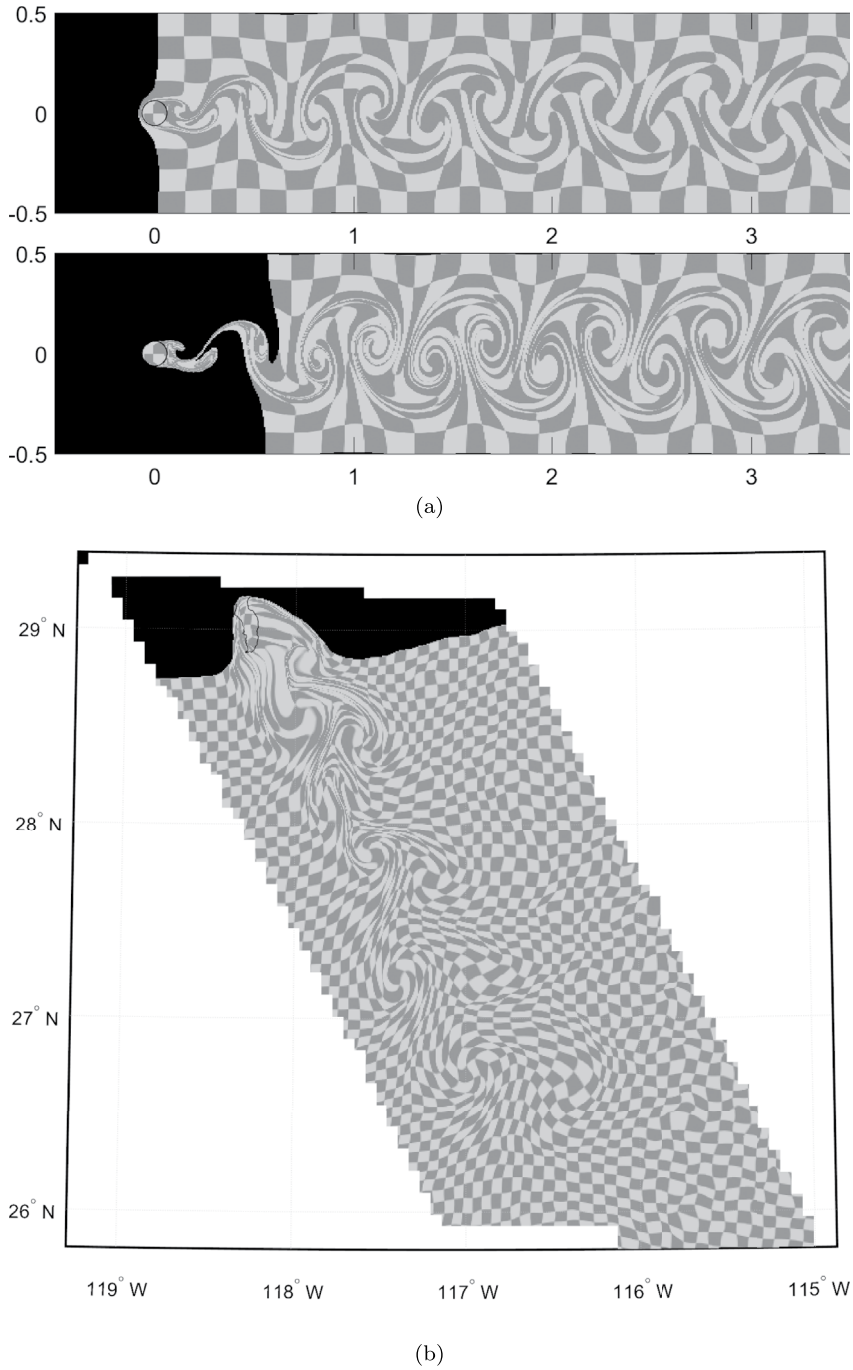

Figure 6. Texture advection of a checkerboard pattern reveals how patches deform during advection. In (a), Cylinder2D flow from $t_0 = 10$ for duration $\tau = 0.5$ (top) and $\tau = 1.0$ (bottom). In (b), Guadalupe flow from $t_0 = 20{:}22$ UTC for $\tau = 02{:}46{:}40$.

Despite their popularity, LICs are limited to the display of streamlines, making them unsuitable for the extraction of dynamical features in time-dependent flow. The LIC images plotted for a given time step in Figures 7a and 7b convey very similar information to the streamlines plotted in Figure 4. Their main advantage is that they cover the entire domain and avoid the seeding problem of the streamlines. While some extensions have been proposed that integrate along pathlines (Shen & Kao, 1997), those are less frequently used. A more common alternative is to subtract the ambient velocity from the flow in order to separate features such as vortices from their movement. In the literature, a number of approaches can be found,

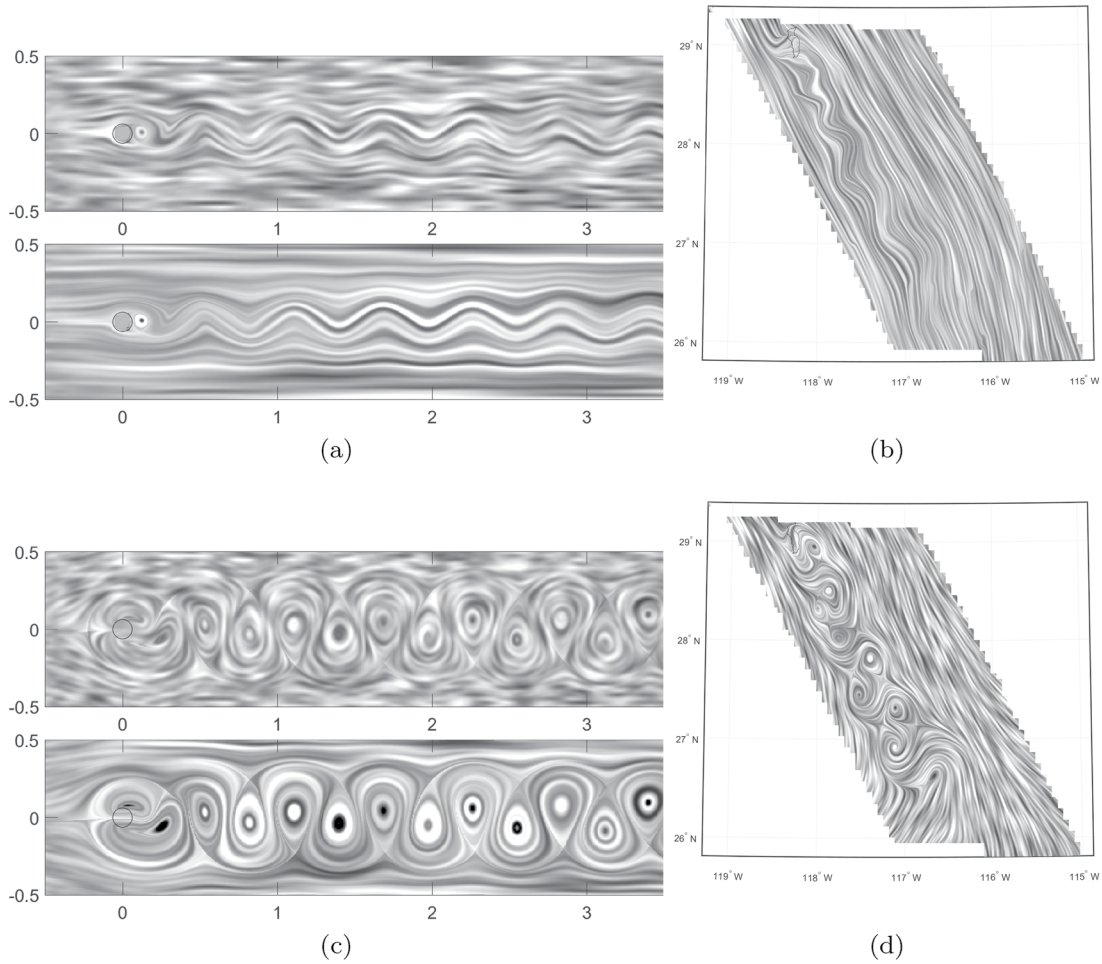

Figure 7. Line integral convolution for the original flows (a and b), and after subtraction of the ambient motion (c and d). The ambient motion describes how flow features are advected. After subtraction, flow features are revealed. In (a) and (c), we see the Cylinder2D flow at time $t_0 = 10$ for $\tau = 0.2$ ((a) top), $\tau = 1.0$ ((a) bottom), $\tau = 0.1$ ((c) top) and $\tau = 0.5$ ((c) bottom). In (b) and (d), the Guadalupe flow at 18:57 UTC is shown.

including the subtraction of an average inflow velocity (Weinkauf et al., 2007), or the harmonic component of a Helmholtz decomposition (Bhatia et al., 2014) to separate external from internal flow behavior. Alternatively, the ambient velocity can be described as the velocity of an observer that moves with flow features such as vortices. Motivated by the seminal observation of Lugt (1979) that there is no single observer that can follow all flow features in the domain at once, Günther, Gross, et al. (2017) searched for an observer locally that sees the vector field in an as-steady-as-possible way. The velocity field seen by this observer thereby becomes approximately steady, making the use of streamlines appropriate to reveal flow features. The result of such an unsteadiness minimization using the spatially varying formulation of Baeza Rojo and Günther (2020) is shown in Figures 7c and 7d, which now reveals the vortices. Similar optimizations have been done globally (Hadwiger et al., 2019) and on general manifolds (Rautek et al., 2021). The optimization of reference frames is numerically challenging, especially on measured data, as it requires accurate derivative estimates. In the following, we move on to feature-based methods that are derived from pathline behavior.

6. Feature-Based Methods

6.1. Lagrangian Coherent Structures

Fluid flows are a continuum of particles. In a flow, there are distinguished sets of particles, so-called material lines, that determine the behavior of the fluid. For a comparative fluid flow analysis, those material

lines are of high interest, since they divide the domain into regions with coherent behavior, which could be compared among given vector fields. For instance, such material lines enclose vortices or denote transport barriers, which are both important objects when studying transport and mixing. In the fluid dynamics literature, these structures are called LCS (Lagrangian Coherent Structures). Recently, Haller (2015) gave a comprehensive overview of the types of LCS and their extraction algorithms. We refer to Onu et al. (2015) for more details on LCS extraction techniques. LCS structures can be derived from variational principles, that is, they are lines that maximize or minimize a certain behavior. Commonly, three types are distinguished:

1. Hyperbolic LCS are material lines that repel or attract particles locally the strongest (Haller, 2011). These lines act as transport barriers and are found by observing flow behavior in forward and backward time.
2. Elliptic LCS are the boundaries of vortices, which have been characterized as lines that bound coherent rotations (Haller et al., 2016), that show no stretching during advection (Serra & Haller, 2016), or that inhibit vorticity diffusion (Katsanoulis et al., 2019).
3. Parabolic LCS are material lines along which material shearing is minimized (Farazmand et al., 2014), which identifies jet cores. In atmospheric flows, they have also been characterized as lines with maximal flow velocity (Kern et al., 2017).

In the following, we take a closer look at vortices and transport barriers, since those are the structures that can be found in Kármán vortex streets.

6.2. Vortices

Vortex measures are categorized into region-based and line-based methods. Region-based methods return a scalar field that expresses how strong the vortical behavior is at a certain location. To extract vortices, a threshold needs to be applied, which is often not easy to set, since vortices decay over time or carry a varying amount of angular momentum throughout the domain. Line-based methods on the other hand return the so-called vortex coreline, which is the line that all other particles swirl around. In the following, we explain two of the most common vortex measures for two-dimensional flows. We refer to Günther and Theisel (2018) for a recent and comprehensive overview of vortex extraction techniques.

One of the most prominent region-based vortex measures is the vorticity scalar field $\omega(x,y)$

$$\omega(x,y) = \frac{\partial v(x,y)}{\partial x} - \frac{\partial u(x,y)}{\partial y} \tag{10}$$

For meteorological flows, we let $\omega(x,y)$ be the vorticity measured relative to the Earth's rotation, which is then also referred to as relative vorticity. The sign of ω determines the rotation direction, whereas the magnitude relates to twice the angular velocity of a virtual tracer particle. It can be seen in Equation 10 that the vorticity field requires an estimation of derivatives, which is challenging in noisy measurement data. It can be expected that the resulting vorticity scalar field contains patches of noise, which in fact are apparent in Figure 8. Rather than spatially averaging the values to remove the noise, as was done in Horváth et al. (2020), it is more suitable to average vorticity values along a pathline over time. This way, long-living vortex structures are revealed and short-lived noise is removed. Vorticity ω is only Galilean invariant–that is, invariant only in an inertial non-accelerating reference frame–because the rotation of an observer adds to the vorticity scalar, which is undesirable since ideally all observers should observe the feature in the same way. Fortunately, the difference between two spatially neighboring vorticity values cancels the added observer rotation, making not only vorticity extrema, but also the deviation of relative vorticity–that is, the difference to the local average vorticity–objective. Haller et al. (2016) proposed the Lagrangian-averaged vorticity deviation, which averages the vorticity deviations along pathlines:

$$\mathrm{LAVD}(\mathbf{x},t;\tau) = \int_t^{t+\tau} |\omega(\Phi_t^{s-t}(\mathbf{x}),s) - \omega_{avg}(\Phi_t^{s-t}(\mathbf{x}),s)|\,\mathrm{d}s \tag{11}$$

where $\omega_{avg}(\mathbf{x},t) = \frac{1}{|U(\mathbf{x})|}\int_{U(\mathbf{x})} \omega(\mathbf{x},t)\mathrm{d}V$ is the average vorticity in a local neighborhood U. LAVD is objective and locates temporally coherent structures. For the Cylinder2D flow in Figure 8a, LAVD (bottom) emphasizes locations that remain for a long time inside a vortex. Thus, the vortices in the immediate wake of the cylinder become more circular than with vorticity (top).

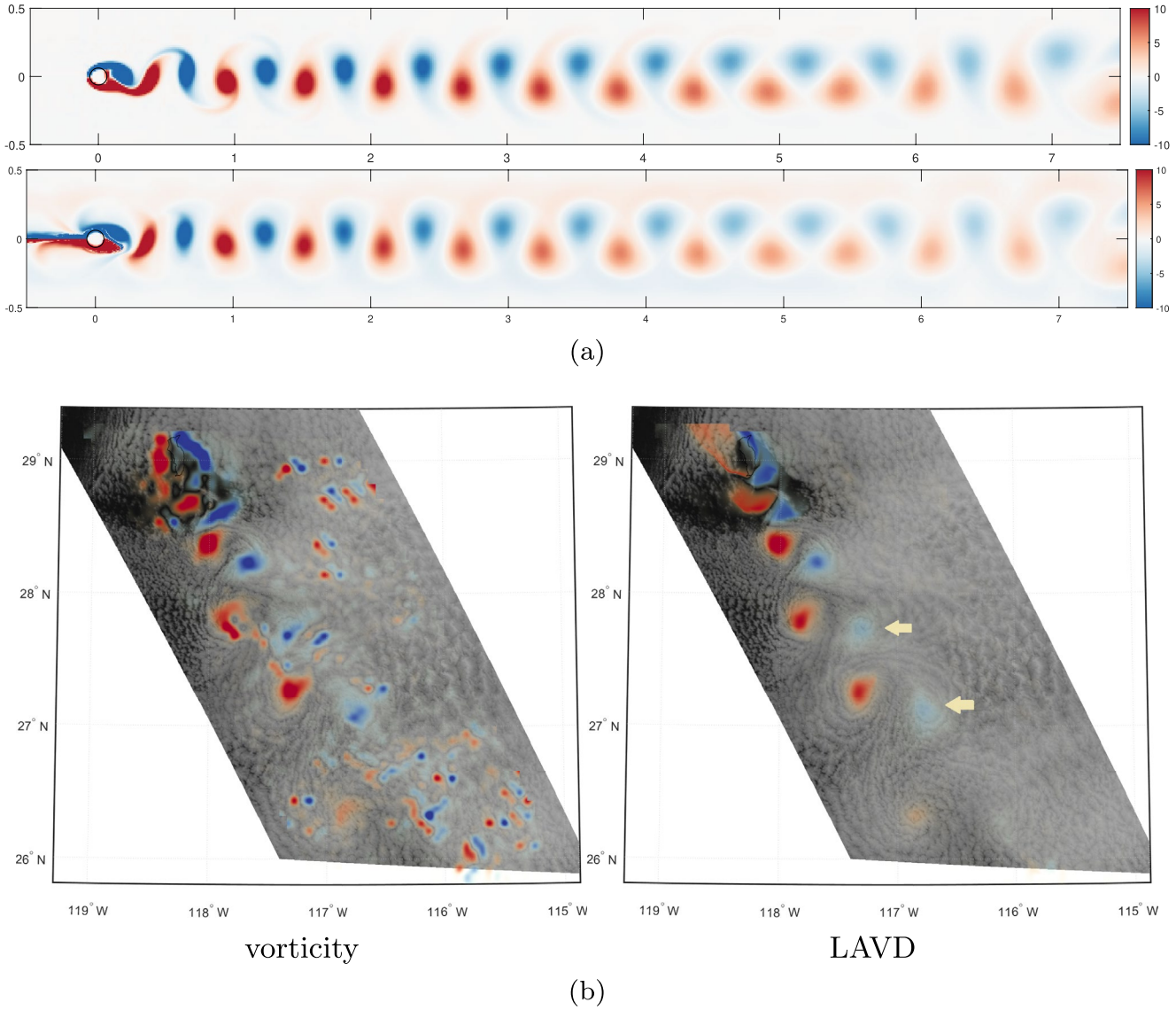

Figure 8. Comparison of vorticity, which is calculated per time slice, with its temporally coherent extension named Lagrangian-averaged vorticity deviation (LAVD). In (a), the Cylinder2D flow is visualized by calculating vorticity (top) at time $t_0 = 12$, and using LAVD (bottom) at $t_0 = 12$, $\tau = 2$, $U = 41 \times 41$ grid points. In (b), the Guadalupe flow is depicted by vorticity (left) at 17:02 UTC and by LAVD (right) from $t_0 =$ 15:47 UTC for duration $\tau =$ 02:46:40 hr and $U = 21 \times 21$ grid points, which covers 252km^2. Vorticity measures the rotations per time unit, whereas LAVD measures the rotations per time unit relative to the neighborhood region.

In the Guadalupe flow, we not only see that LAVD removed the noise successfully, but the vortex locations are also well aligned with the circular cloud patterns. Moreover, the captured vortex decay is asymmetric: anticyclonic vorticity, marked with arrows, decreases significantly faster than cyclonic vorticity, which is apparent by the decreased saturation of the blue color compared to the red color in vortex pairs. Such contrast is detectable in the visual appearance of the vortices too, because anticyclonic eddies have less well-preserved spiral cloud patterns than cyclonic eddies at the same downstream location. As discussed in Horváth et al. (2020), an asymmetric island wake is the expected behavior, predicted by both laboratory experiments and numerical simulations, which arises from the combined effects of Earth's rotation and Guadalupe's nonaxisymmetric shape resembling an inclined flat plate at low angle of attack. The good correspondence between the asymmetric LAVD field and the observed cloud structures indirectly confirms the fidelity of the fluid dynamics embedded in the measured wind field.

6.3. Material Boundaries

When releasing a small group of particles inside a finite-sized sphere, the small sphere is likely to deform under the action of advection over time. Locations at which a sphere elongates locally the strongest are part of a repelling hyperbolic LCS. The opposite attracting hyperbolic LCS are found by observing the transport behavior in backward time. In continuum mechanics, this local deformation is linearly approximated by the right Cauchy-Green deformation tensor:

$$\mathbf{C}(\mathbf{x},t;\tau) = \frac{\partial \mathbf{\Phi}_t^\tau(\mathbf{x})}{\partial \mathbf{x}}^T \frac{\partial \mathbf{\Phi}_t^\tau(\mathbf{x})}{\partial \mathbf{x}} \tag{12}$$

The gradient of the flow map, which is numerically calculated by central differences, is multiplied with its transpose to make this deformation measure invariant under rotations of the observer. The largest eigenvalues of this tensor (λ_{max}) encode the strongest linear elongation. Introducing normalizations to account for the squaring of the gradient in Equation 12, the exponentional separation rate, and the continued growth over the duration τ, leads to the finite-time Lyapunov exponent FTLE (Haller, 2001; Shadden et al., 2005):

$$\mathrm{FTLE}(\mathbf{x},t;\tau) = \frac{1}{|\tau|}\ln\sqrt{\lambda_{max}(\mathbf{C}(\mathbf{x},t;\tau))} \tag{13}$$

Ridges in this scalar field are frequently used as approximations to hyperbolic LCS. Figure 9 depicts forward FTLE (repelling behavior) and backward FTLE (attracting behavior) in the Cylinder2D and the Guadalupe flows. Attracting FTLE ridges are computed by backward integration within a time span $[t-\tau,t]$, that is, they reveal structures that have formed in the past up until the current time t. The alignment of the attracting FTLE ridges in the Guadalupe flow with the cloud patterns shows that the transport dynamics of the satellite-measured wind field are in agreement with the observed organization of clouds. Repelling FTLE ridges are computed by forward integration within a time span $[t,t+\tau]$, that is, they indicate regions that will show repelling behavior in the future. Figure 10 illustrates how these ridges can be interpreted. In a Kármán vortex street, the strongest repelling ridges (red) arise from particles that attract onto (or toward) an attracting FTLE ridge (blue), but will then separate in opposite directions along the blue FTLE ridge, as the separating particles get curled up in different vortices (orange). The red ridge line and the blue ridge line thereby separate vortex regions. In topological terms, the intersection of the red and blue ridge lines results in a bifurcation point.

6.4. Space-Time Mapping

Time-dependent 2D flows have three dependent variables: the position coordinates x and y, and the time . A rather natural form to visualize a time-dependent flow is to visualize each time slice independently and play the time series as a video. This form of animation is suitable to show the instantaneous changes around the currently observed time slices, but is not very effective in communicating motions that occurred across larger time spans, such as the path of a vortex in our vortex street. For such a 2D time-dependent flow, we can lift the domain one dimension up by mapping the time to the third spatial dimension, which leads to a so-called space-time visualization. We will denote a coordinate in space-time with $\overline{\mathbf{x}} = (\mathbf{x},t)$, which incidentally also describes a coordinate in the phase space of a particle, thus making this a space that captures all dimensions of the dynamical system. There are two common space-time velocity fields that can be derived from the unsteady vector field, see Theisel et al. (2004):

$$\overline{\mathbf{s}}(\overline{\mathbf{x}}) = \frac{\mathrm{d}}{\mathrm{d}t}\begin{pmatrix} x \\ y \\ t \end{pmatrix} = \begin{pmatrix} u(x,y,t) \\ v(x,y,t) \\ 0 \end{pmatrix} \qquad \overline{\mathbf{p}}(\overline{\mathbf{x}}) = \frac{\mathrm{d}}{\mathrm{d}t}\begin{pmatrix} x \\ y \\ t \end{pmatrix} = \begin{pmatrix} u(x,y,t) \\ v(x,y,t) \\ 1 \end{pmatrix} \tag{14}$$

which differ in the rate of change of the last dimension, that is, the time. The tangent curves in the field $\overline{\mathbf{s}}(\overline{\mathbf{x}})$ are streamlines, whereas the tangent curves of $\overline{\mathbf{p}}(\overline{\mathbf{x}})$ are pathlines. A direct visualization of the flow features in these two fields immediately shows streamline-oriented and pathline-oriented vector field topology. For fluid flows, we are primarily interested in $\overline{\mathbf{p}}(\overline{\mathbf{x}})$. Due to the mapping of the time axis to the third spatial dimension, the paths of vortices, later extracted as extremal lines of the LAVD field, become quickly apparent. For an introduction to the rendering and extraction of extremal features, we refer to Kindlmann et al. (2018).

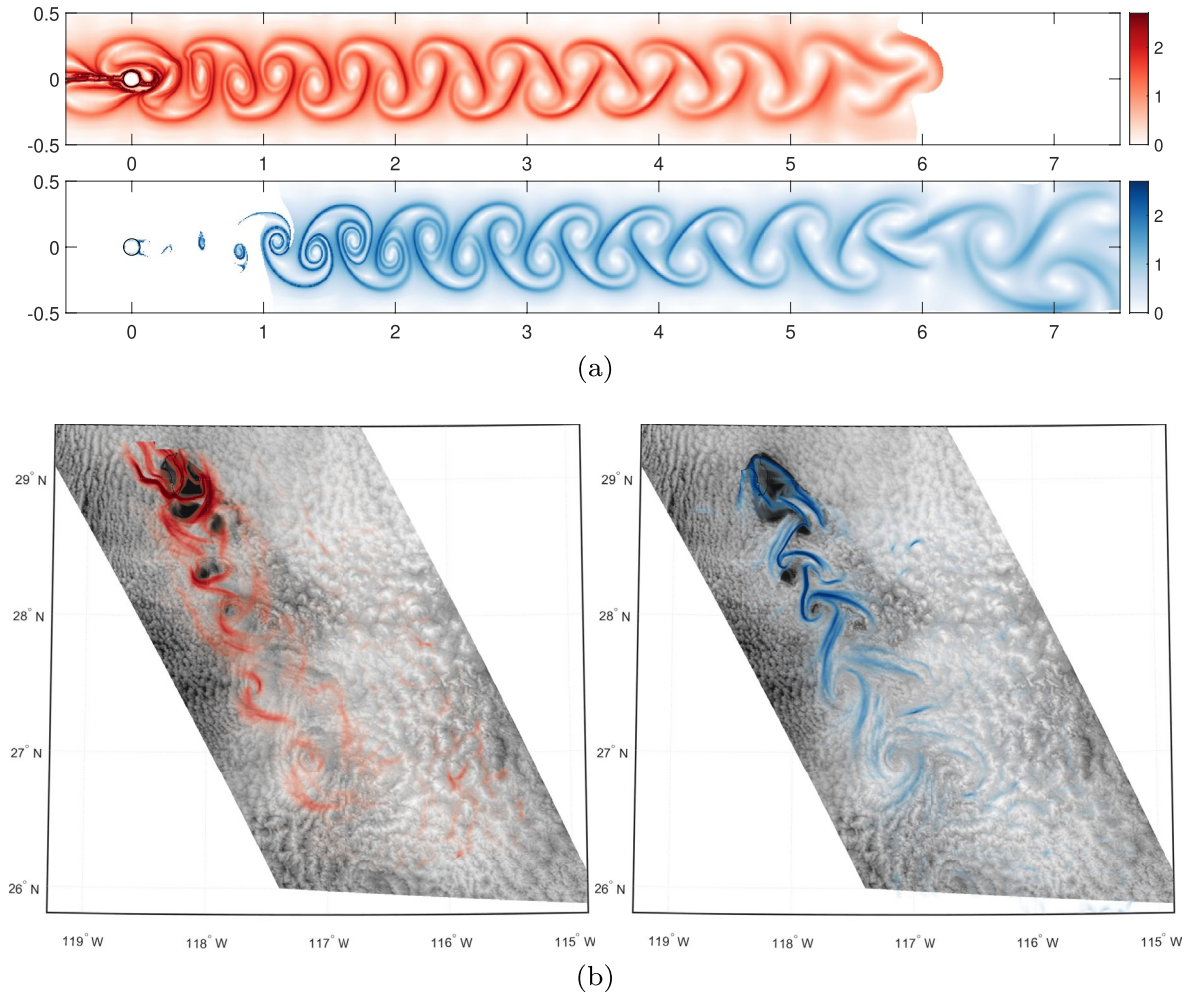

Figure 9. The finite-time Lyapunov exponent reveals attracting (backward FTLE, blue) and repelling (forward FTLE, red) material lines in the domain that strongly influence the passive transport of particles. In the Cylinder2D flow, slice $t_0 = 10$ is shown with an FTLE integration duration of $\tau = 1.5$. The Guadalupe flow is displayed at time $t_0 =$ 18:22 UTC with an FTLE integration duration of $\tau =$ 02:46:40 hr, both forward and backward. FTLE measures the linearized stretching rate on logarithmic scale per finite time interval τ.

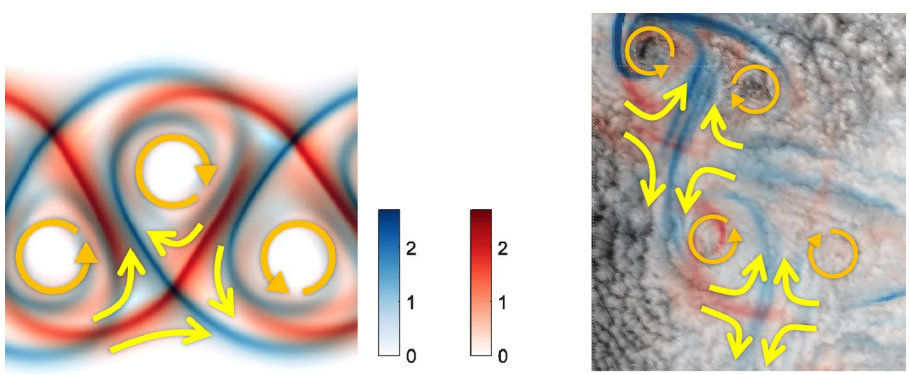

Figure 10. Ridge lines in the finite-time Lyapunov exponent (repelling in red, attracting in blue) separate the fluid domain into regions. Here, yellow arrows indicate the relative particle motion. In a Kármán vortex street, the separate regions may contain vortices (orange). The left panel shows the Cylinder2D flow and the right panel shows the Guadalupe flow using the same parameters as in Figure 9.

In Figure 11, the previously introduced feature extraction methods are used to assess the quality of the vector field that was reconstructed from measured cloud motion. In Figure 11a, the visible band satellite image of the vortex street is overlayed with the elliptic LCS (in terms of LAVD) and attracting hyperbolic LCS (in terms of backward FTLE). We can clearly see that the emergence of patterns in the cloud field is constrained by and organized around the LCS, which provides strong evidence that the retrieved vector field exhibits the same fluid dynamical processes that the real-world clouds actually experienced. The space-time visualization in Figure 11b further sheds light onto the temporal evolution of the vortices, with the blue axis denoting time. In the first time step (bottom slice), the vortices are neatly organized in the common Kármán vortex street pattern. As time progresses, vortex 4 is pushed eastwards by a crosswind, where it blocks the path of vortex 3. As a result, vortex 3 quickly weakens and gets overtaken by vortex 1. Additionally, the space-time visualization makes the temporal stability of the extracted paths apparent, as the space-time curves are smooth and without noise.

6.5. Discussion

Derived features, such as region-based vortex measures or the FTLE field as indicator for hyperbolic LCS, are not only useful for a qualitative visual comparison, but can also be useful for a feature-centered quantitative evaluation. In both flow visualization and fluid dynamics, two important properties have been recognized as essential characteristics that flow features should possess. First, the features should be seen by all rotating and translating observers in an equal manner, their motion notwithstanding, which is referred to as objectivity. Both LAVD and FTLE fulfill this property. Second, a Lagrangian coherent feature should–as the name suggests–be coherent when observed along pathlines over time. Thus, both LAVD and FTLE measure the fluid behavior over a certain time window. The length of this time window, thereby remains a crucial user parameter. A limitation of both LAVD and FTLE is that it is unclear where along the pathline the characteristic feature behavior was observed. For example, consider pathlines that stay close together most of the time and only separate strongly toward the end of the set time interval. This delayed separation is not immediately visible from the scalar field alone and is only revealed when the parameter-dependence of the features is explored, cf. Sagristà et al. (2020) for parameter analysis tools. Alternatively, features could be extracted locally per time slice and joined afterward in time to precisely determine the beginning and end of a feature's life time. The latter motivates ongoing research on the temporally local analysis of time-dependent vector field topology (Baeza Rojo & Günther, 2020), which could deliver another set of features useful for a comparative analysis of scalar and vector fields. This direction of research is left for future work.

At present, we assumed that cloud motion is governed by passive particle motion, that is, the clouds move strictly in the direction of the vector field. Since the vector field is derived from the visible cloud patterns, this assumption is reasonable. Also note that the passive tracer assumption is the norm in all operational cloud-motion wind algorithms. However, if clouds were modeled as active tracers, the underlying flow field would be different. In that case, cloud dynamics would have to be calculated from an active particle model, the parameters of which are not trivial to determine. This has already been done in other application domains, for example by defining flow maps based on inertial particle models for bubbles or sand, which are easier to derive (Günther & Theisel, 2017). FTLE and LAVD are, however, straightforward to extend to active particle models.

7. Conclusions

With the advent of the latest generation geostationary imagers, such as ABI on GOES-R, satellite wind retrievals on the km and minute scale have become a reality. These high spatiotemporal-resolution winds enable the study of mescoscale geophysical flows and are also in increasing demand as input data for the ever-finer resolution operational forecast models. However, the visualization and validation–or at least consistency test–of these data sets is challenging and progress on these fronts will require moving beyond traditional techniques, such as grid point-based comparisons to radiosonde, aircraft, or reanalysis winds. To this end, we demonstrated advanced visualization and dynamical system analysis tools through the example of a high-resolution GOES-16 wind data set that captures an atmospheric Kármán vortex street in the lee of Guadalupe.

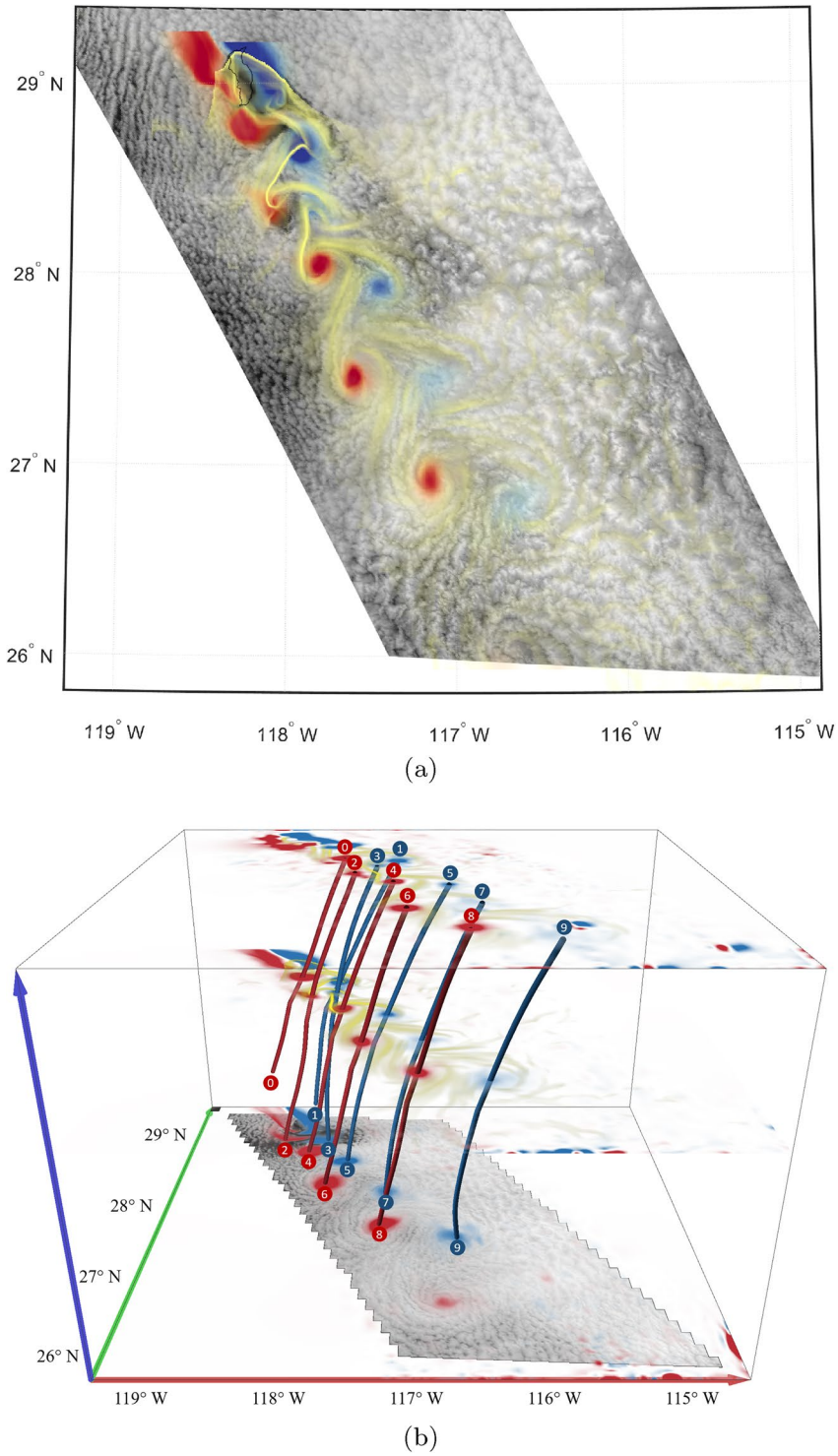

Figure 11. Feature-based quality assessment of the Guadalupe velocity field obtained by cloud tracking. In (a), overlaying vortices (Lagrangian-averaged vorticity deviation [LAVD] in red/blue) and attracting transport barriers (backward finite-time Lyapunov exponent [FTLE] in yellow) on visible imagery shows the agreement of the retrieved fluid dynamical processes with the observed cloud patterns. Here, at t_0 = 18:22 UTC for an FTLE and LAVD integration duration of τ = 02:46:40. In (b), a space-time mapping of the flow reveals temporally coherent vortex paths with FTLE time slices from bottom to top at 14:32, 19:22, and 22:37 UTC.

The fluid dynamics of the reconstructed vector field should give rise to flow features that correlate with the observed mesoscale cloud patterns, since those patterns are the result of a fluid dynamical evolution. We discussed the advantages and disadvantages of various visualization approaches. Direct methods such as arrow plots are able to show noise in the data, but are obscured by the ambient motion of features in time-dependent flow. Geometry-based methods (integral curves) require careful seeding and are primarily useful for qualitative analysis, and when shown in combination with an underlying scalar field that makes use of the non-occluded spaces. Texture-based techniques such as texture advection and LIC convey information more densely, but especially LIC must be used with care, since it displays streamlines, which are non-physical unless observed in a suitable unsteadiness-minimizing reference frame. Feature-based methods such as LAVD and FTLE, however, reveal LCS that drive the fluid dynamical processes. Both of the latter approaches are objective and incorporate the desirable temporal coherence of the features in question.

The LAVD and FTLE fields computed from the GOES-16 winds align well with the observed mushroom cloud patterns of the vortex street, indirectly validating the satellite retrievals. In the current introductory study, the comparison of observed and derived structures was qualitative (visual) only. Turning these methods into useful validation tools will, however, require putting the comparison on a quantitative basis, which is a non-trivial task. Fortunately, there are promising candidate metrics from the field of feature-based spatial forecast verification, which operate precisely on the type of coherent objects that are represented by the LCS of the flow. The FTLE ridges can be extracted from the satellite-retrieved wind field and then quantitatively compared to detected ridges in cloud images, using for instance the SAL technique (Wernli et al., 2008), which assesses the structure (size and shape), amplitude, and location of the identified objects. Other quantitative metrics could also be derived based on the presence and distance of vortices and transport barriers.

The validation of mesoscale numerical models can also benefit from a comparison between the simulated and observed Lagrangian structures. In the next step, we will evaluate the ability of Weather Research and Forecasting model simulations to reproduce the satellite-retrieved LCS of the Guadalupe vortex street and investigate model sensitivity to the used boundary layer scheme, based on such feature-centered quality metrics.

Data Availability Statement

The GOES-16 ABI L1b radiances are available from the NOAA Comprehensive Large Array-data Stewardship System (CLASS) archive (https://www.avl.class.noaa.gov). The high-resolution GOES-16 wind retrievals are available from the Zenodo data repository (https://doi.org/10.5281/zenodo.3534276). The code to reproduce the images in the study, as well as the data can be found online at https://github.com/tobguent/vislcs-guadalupe.

Acknowledgments
The work of T. Günther was supported by the Swiss National Science Foundation (SNSF) Ambizione grant no. PZ00P2_180114. The work of A. Horváth was supported by German Federal Ministry of Education and Research (BMBF) project HD(CP)2 (contract O1LK1505D) and by Deutsche Forschungsgemeinschaft (DFG) project VolImpact/VolPlume (contract BU 2253/7-1). With this work the authors contribute to the Cluster of Excellence "CLICCS—Climate, Climatic Change, and Society" funded by DFG (EXC 2037, Project Number 390683824), and to the Center for Earth System Research and Sustainability (CEN) of Universität Hamburg. Open access funding enabled and organized by Projekt DEAL.

References

Baeza Rojo, I., & Günther, T. (2020). Vector field topology of time-dependent flows in a steady reference frame. *IEEE Transactions on Visualization and Computer Graphics*, *26*(1), 280–290. https://doi.org/10.1109/TVCG.2019.2934375

Bhatia, H., Pascucci, V., Kirby, R. M., & Bremer, P.-T. (2014). Extracting features from time-dependent vector fields using internal reference frames. *Computer Graphics Forum*, *33*(3), 21–30. https://doi.org/10.1111/cgf.12358

Borgo, R., Kehrer, J., Chung, D. H. S., Maguire, E., Laramee, R. S., Hauser, H., & Chen, M. (2013). Glyph-based Visualization: Foundations, Design Guidelines, Techniques and Applications. In M. Sbert, & L. Szirmay-Kalos (Eds.), *Eurographics 2013 — state of the art reports*. The Eurographics Association. https://doi.org/10.2312/conf/EG2013/stars/039-063

Bresky, W., Daniels, J., Wanzong, S., & Wanzong, S. T. (2012). New methods toward minimizing the slow speed bias associated with atmospheric motion vectors. *Journal of Applied Meteorology and Climatology*, *51*(12), 2137–2151. https://doi.org/10.1175/JAMC-D-11-0234.1

Bujack, R., & Middel, A. (2020). State of the art in flow visualization in the environmental sciences. *Environmental Earth Sciences*, *79*(2), 1–10. https://doi.org/10.1007/s12665-019-8800-4

Cabral, B., & Leedom, L. (1993). Imaging vector fields using line integral convolution. *Computer Graphics*, *27*, 263–272. https://doi.org/10.1145/166117.166151

Chen, Y., Cohen, J., & Krolik, J. (2007). Similarity-guided streamline placement with error evaluation. *IEEE Transactions on Visualization and Computer Graphics*, *13*, 1448–1455. https://doi.org/10.1109/tvcg.2007.70595

Chopra, K. P., & Hubert, L. F. (1965). Mesoscale eddies in wakes of islands. *Journal of the Atmospheric Sciences*, *22*(6), 652–657. https://doi.org/10.1175/1520-0469(1965)022<0652:meiwoi>2.0.co;2

Cimbala, J. M., Nagib, H. M., & Roshko, A. (1988). Large structure in the far wakes of two-dimensional bluff bodies. *Journal of Fluid Mechanics*, *190*, 265–298. https://doi.org/10.1017/S0022112088001314

Daniels, J., Bresky, W., Wanzong, S., Velden, C., & Berger, H. (2010). *Goes-r advanced baseline imager (abi) algorithm theoretical basis document for derived motion wind*. GOES-R Program Office. Retrieved from https://www.star.nesdis.noaa.gov/goesr/documents/ATBDs/Baseline/ATBD_GOES-R_Winds_v3.1_Feb2019.pd

Farazmand, M., Blazevski, D., & Haller, G. (2014). Shearless transport barriers in unsteady two-dimensional flows and maps. *Physica D: Nonlinear Phenomena*, *278*, 44–57. https://doi.org/10.1016/j.physd.2014.03.008

Günther, T., & Baeza Rojo, I. (2021). Introduction to vector field topology. In *Topological methods in data analysis and visualization vi*. Springer.

Günther, T., Gross, M., & Theisel, H. (2017). Generic objective vortices for flow visualization. *ACM Transactions on Graphics*, *36*(4), 141. https://doi.org/10.1145/3072959.3073684

Günther, T., & Theisel, H. (2017). Backward finite-time lyapunov exponents in inertial flows. *IEEE Transactions on Visualization and Computer Graphics*, *23*(1), 970–979. https://doi.org/10.1109/TVCG.2016.2599016

Günther, T., & Theisel, H. (2018). The state of the art in vortex extraction. *Computer Graphics Forum*, *37*(6), 149–173. https://doi.org/10.1111/cgf.13319

Günther, T., Theisel, H., & Gross, M. (2017). Decoupled opacity optimization for points, lines and surfaces. *Computer Graphics Forum*, *36*, 153–162. https://doi.org/10.1111/cgf.13115

Hadwiger, M., Mlejnek, M., Theußl, T., & Rautek, P. (2019). Time-dependent flow seen through approximate observer killing fields. *IEEE Transactions on Visualization and Computer Graphics (Proceedings IEEE Scientific Visualization 2018)*, *25*(1), 1257–1266. https://doi.org/10.1109/tvcg.2018.2864839

Haller, G. (2001). Distinguished material surfaces and coherent structures in three-dimensional fluid flows. *Physica D: Nonlinear Phenomena*, *149*(4), 248–277. https://doi.org/10.1016/S0167-2789(00)00199-8

Haller, G. (2011). A variational theory of hyperbolic Lagrangian coherent structures. *Physica D: Nonlinear Phenomena*, *240*(7), 574–598. https://doi.org/10.1016/j.physd.2010.11.010

Haller, G. (2015). Lagrangian coherent structures. *Annual Review of Fluid Mechanics*, *47*, 137–162. https://doi.org/10.1146/annurev-fluid-010313-141322

Haller, G., Hadjighasem, A., Farazmand, M., & Huhn, F. (2016). Defining coherent vortices objectively from the vorticity. *Journal of Fluid Mechanics*, *795*, 136–173. https://doi.org/10.1017/jfm.2016.151

Heinze, R., Raasch, S., & Etling, D. (2012). The structure of kármán vortex streets in the atmospheric boundary layer derived from large eddy simulation. *Meteorologische Zeitschrift*, *21*(3), 221–237. https://doi.org/10.1127/0941-2948/2012/0313

Holmlund, K., Velden, C. S., & Rohn, M. (2001). Enhanced automated quality control applied to high-density satellite winds. *Monthly Weather Review*, *129*, 517–529. https://doi.org/10.1175/1520-0493(2001)129<0517:eaqcat>2.0.co;2

Horváth, Á. (2013). Improvements to misr stereo motion vectors. *Journal of Geophysical Research: Atmospheres*, *118*, 5600–5620. https://doi.org/10.1002/jgrd.50466

Horváth, Á., Bresky, W., Daniels, J., Vogelzang, J., Stoffelen, A., Carr, J., et al. (2020). Evolution of an atmospheric kármán vortex street from high-resolution satellite winds: Guadalupe island case study. *Journal of Geophysical Research: Atmospheres*, *125*(4), e2019JD032121. https://doi.org/10.1029/2019JD032121

Hubert, L. F., & Krueger, A. F. (1962). Satellite pictures of mesoscale eddies. *Monthly Weather Review*, *90*(11), 457–463. https://doi.org/10.1175/1520-0493(1962)090<0457:spome>2.0.co;2

Jobard, B., & Lefer, W. (1997). Creating evenly-spaced streamlines of arbitrary density. *Proceedings of Eurographics Workshop on Visualization in Scientific Computing*, *7*, 45–55. https://doi.org/10.1007/978-3-7091-6876-9_5

Katsanoulis, S., Farazmand, M., Serra, M., & Haller, G. (2019). *Vortex boundaries as barriers to diffusive vorticity transport in two-dimensional flows*. Retrieved from https://doi.org/10.1103/PhysRevFluids.5.024701

Kern, M., Hewson, T., Sadlo, F., Westermann, R., & Rautenhaus, M. (2017). Robust detection and visualization of jet-stream core lines in atmospheric flow. *IEEE Transactions on Visualization and Computer Graphics*, *24*(1), 893–902.

Kindlmann, G., Chiw, C., Huynh, T., Gyulassy, A., Reppy, J., & Bremer, P.-T. (2018). Rendering and extracting extremal features in 3d fields. *Computer Graphics Forum*, *37*(3), 525–536. https://doi.org/10.1111/cgf.13439

Laidlaw, D. H., Kirby, R. M., Jackson, C. D., Davidson, J. S., Miller, T. S., da Silva, M., et al. (2005). Comparing 2d vector field visualization methods: A user study. *IEEE Transactions on Visualization and Computer Graphics*, *11*(1), 59–70. https://doi.org/10.1109/TVCG.2005.4

Lugt, H. J. (1979). The dilemma of defining a vortex. In U. Müller, K. G. Roesner, & B. Schmidt (Eds.), *Recent developments in theoretical and experimental fluid mechanics: Compressible and incompressible flows* (pp. 309–321). Berlin, Heidelberg: Springer Berlin Heidelberg. https://doi.org/10.1007/978-3-642-67220-0_32

Lyons, W. A., & Fujita, T. (1968). Mesoscale motions in oceanic stratus as revealed by satellite data. *Monthly Weather Review*, *96*(5), 304–314. https://doi.org/10.1175/1520-0493(1968)096<0304:mmiosa>2.0.co;2

MacCormack, R. W. (2002). The effect of viscosity in hypervelocity impact cratering. In *Frontiers of computational fluid dynamics* (pp. 27–43). https://doi.org/10.1142/9789812810793_0002

Mattausch, O., Theußl, T., Hauser, H., & Gröller, E. (2003). Strategies for interactive exploration of 3D flow using evenly-spaced illuminated streamlines. In *Proceedings spring conference on computer graphics (sscg)* (pp. 213–222). ACM. https://doi.org/10.1145/984952.984987

McLoughlin, T., Laramee, R. S., Peikert, R., Post, F. H., & Chen, M. (2010). Over two decades of integration-based, geometric flow visualization. *Computer Graphics Forum*, *29*(6), 1807–1829. https://doi.org/10.1111/j.1467-8659.2010.01650.x

Nunalee, C. G., & Basu, S. (2014). On the periodicity of atmospheric von kármán vortex streets. *Environmental Fluid Mechanics*, *14*(6), 1335–1355. https://doi.org/10.1007/s10652-014-9340-9

Nunalee, C. G., Horváth, Á., & Basu, S. (2015). High-resolution numerical modeling of mesoscale island wakes and sensitivity to static topographic relief data. *Geoscientific Model Development*, *8*(8), 2645–2653. https://doi.org/10.5194/gmd-8-2645-2015

Onu, K., Huhn, F., & Haller, G. (2015). LCS tool: A computational platform for Lagrangian coherent structures. *Journal of Computational Science*, *7*, 26–36. https://doi.org/10.1016/j.jocs.2014.12.002

Pilar, D. H., & Ware, C. (2013). Representing flow patterns by using streamlines with glyphs. *IEEE Transactions on Visualization and Computer Graphics*, *19*(8), 1331–1341. https://doi.org/10.1109/TVCG.2013.10

Popinet, S. (2003). Gerris: A tree-based adaptive solver for the incompressible euler equations in complex geometries. *Journal of Computational Physics*, *190*(2), 572–600. https://doi.org/10.1016/s0021-9991(03)00298-5

Rautek, P., Mlejnek, M., Beyer, J., Troidl, J., Pfister, H., Theußl, T., & Hadwiger, M. (2021). Objective observer-relative flow visualization in curved spaces for unsteady 2d geophysical flows. *IEEE Transactions on Visualization and Computer Graphics*, *27*(2). https://doi.org/10.1109/tvcg.2020.3030454

Sagristà, A., Jordan, S., & Sadlo, F. (2020). Visual analysis of the finite-time lyapunov exponent. *Computer Graphics Forum*, *39*(3), 331–342. https://doi.org/10.1111/cgf.13984

Sane, S., Bujack, R., Garth, C., & Childs, H. (2020). A survey of seed placement and streamline selection techniques. *Computer Graphics Forum*, *39*(3), 785–809. https://doi.org/10.1111/cgf.14036

Serra, M., & Haller, G. (2016). Objective Eulerian coherent structures. Chaos. *An Interdisciplinary Journal of Nonlinear Science*, *26*(5), 053110. https://doi.org/10.1063/1.4951720

Shadden, S. C., Lekien, F., & Marsden, J. E. (2005). Definition and properties of Lagrangian coherent structures from finite-time Lyapunov exponents in two-dimensional aperiodic flows. *Physica D: Nonlinear Phenomena*, *212*(3–4), 271–304. https://doi.org/10.1016/j.physd.2005.10.007

Shen, H.-W., & Kao, D. L. (1997). Uflic: A line integral convolution algorithm for visualizing unsteady flows. *Proceedings. visualization, '97*(Cat. no. 97cb36155), 317–322. https://doi.org/10.1109/VISUAL.1997.663898

Theisel, H., Weinkauf, T., Hege, H.-C., & Seidel, H.-P. (2004). Stream line and path line oriented topology for 2d time-dependent vector fields. *Proceedings. IEEE visualization 2004*, 321–238.

Truesdell, C., & Noll, W. (1965). *The nonlinear field theories of mechanics*. In S. Flugge (Ed.), *Handbuch der Physik, Band III/3*. Berlin: Springer-Verlag.

Van Dyke, M. (1982). *An album of fluid motion*.

Vogelzang, J., Stoffelen, A., Lindsley, R. D., Verhoef, A., & Verspeek, J. (2017). The ascat 6.25 km wind product. *IEEE Journal of Selected Topics in Applied Earth Observations and Remote Sensing*, *10*(5), 2321–2331. https://doi.org/10.1109/JSTARS.2016.2623862

Weinkauf, T., Hege, H.-C., & Theisel, H. (2012). Advected tangent curves: A general scheme for characteristic curves of flow fields. *Computer Graphics Forum*, *31*(2pt4), 825–834. https://doi.org/10.1111/j.1467-8659.2012.03063.x

Weinkauf, T., Sahner, J., Theisel, H., & Hege, H. (2007). Cores of swirling particle motion in unsteady flows. *IEEE Transactions on Visualization and Computer Graphics*, *13*(6), 1759–1766. https://doi.org/10.1109/TVCG.2007.70545

Wernli, H., Paulat, M., Hagen, M., & Frei, C. (2008). Sal—A novel quality measure for the verification of quantitative precipitation forecasts. *Monthly Weather Review*, *136*(11), 4470–4487. https://doi.org/10.1175/2008MWR2415.1

Ye, X., Kao, D., & Pang, A. (2005). Strategy for seeding 3D streamlines. *IEEE Visualization Conference*, *1*, 471–478. https://doi.org/10.1109/VIS.2005.92

Young, G. S., & Zawislak, J. (2006). An observational study of vortex spacing in island wake vortex streets. *Monthly Weather Review*, *134*(8), 2285–2294. https://doi.org/10.1175/MWR3186.1

Yu, H., Wang, C., Shene, C.-K., & Chen, J. (2012). Hierarchical streamline bundles. *IEEE Transactions on Visualization and Computer Graphics*, *18*(8), 1353–1367. https://doi.org/10.1109/TVCG.2011.155